Active material utilization and capacity of fiber-based battery electrodes

Zhuo, Mingzhao; Grazioli, Davide; Simone, Angelo

DOI
10.1016/j.electacta.2019.134929

Publication date
2020

Document Version
Final published version

Published in
Electrochimica Acta

Electrochimica Acta 333 (2020) 134929

Contents lists available at ScienceDirect

Electrochimica Acta

journal homepage: www.elsevier.com/locate/electacta

Active material utilization and capacity of fiber-based battery electrodes

Mingzhao Zhuo [a, *], Davide Grazioli [a], Angelo Simone [a, b]

[a] Faculty of Civil Engineering and Geosciences, Delft University of Technology, Delft, The Netherlands
[b] Department of Industrial Engineering, University of Padova, Padua, Italy

ARTICLE INFO

Article history:
Received 28 August 2019
Received in revised form
20 September 2019
Accepted 21 September 2019
Available online 27 September 2019

Keywords:
Fiber-based composite electrode
Active material utilization
Optimal active-conductive material ratio
Fiber orientation effect
Resistor network model

ABSTRACT

This study presents a three-dimensional computational model to evaluate effective conductivity and capacity of fiber-based battery electrodes. We employ electrodes composed of conductive and active material nanofibers dispersed in an electrolyte matrix. The effective conductivity is calculated by means of an equivalent resistor network model, while capacity evaluation is based on the identification of active material fibers that are accessible to electrons (*i.e.*, those connected with the electronically conductive network). When a constraint is applied to the total fiber content, an optimal active-conductive material ratio is determined that maximizes the active material utilization and the electrode capacity. We also study fiber orientation effects on the electrode electrochemical properties. It is found that fiber orientation has a strong impact on the percolation threshold, and this impact also reflects on the active material utilization: the more the fiber orientation deviates from the ideal isotropic distribution, the lower the utilization of active material fibers. This is of special interest for practical applications where geometrical constraints on fiber orientation arise, as in the case of electrospun fibers deposited on a substrate. The results of this study are therefore meant to give an insight into how a fibrous electrode architecture performs and suggest effective design solutions.

1. Introduction

Electrospun nanofibers improve the electrochemical performance of a battery cell when used in electrodes [1–3] in place of traditional particles. Numerical simulations of the electrochemical processes taking place in traditional battery electrodes at the microstructural level [4] require the solution of sets of coupled differential equations and are computationally demanding. In addition to this, the microstructural analysis of fiber-based electrodes requires the discretization of each fiber, increasing the computational burden to such an extent that the solution of the problem becomes unfeasible for practical purposes. Here, we propose a numerical approach that enables estimation of effective conductivity and capacity from the fiber spatial arrangement.

For the improved performance of energy storage devices, a new avenue has opened up by the use of electrode materials shaped as fibers [1–3,5–7]. Metallic [8] or carbonaceous [9–11] fibers are already employed to enhance the electronic conductivity of battery electrodes. Experimental studies show that conductive material fibers, which will be referred to as “conductive fibers” in this paper, help achieve electrode percolation using less conductive material [8,9] and improve the electrolyte ionic conductivity by creating preferential paths for ionic transport along their surfaces [9]. However, the production of fibers for battery applications is not limited to conductive materials. Thanks to electrospinning, a wide range of anode [11–16] and cathode [13–17] active materials can nowadays be prepared in fiber form and used in full-cell battery configurations [13–16]. The reduced dimensions of nanofibers ensure shorter diffusion paths and higher surface-to-volume ratio relative to the traditional particle morphology, leading to improved capacity, higher charge/discharge rate capabilities, and extended cycle life of the electrodes [1,2]. Despite these advantages, the adoption of active material fibers, which will be referred to as “active fibers” in this paper, does not necessarily lead to discarding electronic conductivity enhancers [14–17]. In this study we ideally replace active fiber-conductive particle electrode architectures with all-fiber (*i.e.*, active fiber-conductive fiber) electrode architectures and evaluate the relationship between the active-

* Corresponding author.
E-mail addresses: m.zhuo@tudelft.nl (M. Zhuo), d.grazioli@tudelft.nl (D. Grazioli), angelo.simone@unipd.it, a.simone@tudelft.nl (A. Simone).

https://doi.org/10.1016/j.electacta.2019.134929

Nomenclature

ΔU	electric potential difference
ϕ	volume fraction
ϕ_a	volume fraction of active fibers
ϕ_a^{eff}	volume fraction of effective active fibers
ϕ_{cr}	critical conductive fiber volume fraction at percolation
ϕ_c	volume fraction of conductive fibers
ϕ_e	volume fraction of the electrolyte
ϕ_p	optimal conductive fiber volume fraction
ϕ_t	total active and conductive fiber volume fraction
φ	azimuthal angle
ρ_a	mass density of the active material
ρ_c	mass density of the conductive material
ϱ	resistivity of the conductive fibers
σ_{eff}	effective conductivity
θ	polar angle
θ_m	limit value of polar angle
A	cross-sectional area of the simulation box
C	total electrode effective capacity
d	fiber diameter
d_α	diameter of fiber α
d_a	active fiber diameter
d_c	conductive fiber diameter
h	shortest distance between two fibers
I_{eff}	total current flowing through the box along one axis
l	fiber length
l_a	active fiber length
l_c	conductive fiber length
L	simulation box edge length
m_A	number of simulation boxes
m_B	number of critical fiber number N_{cr}
n	successfully percolated box number
n_a	active fiber configurations
n_c	conductive fiber configurations
N	fiber number
N_a	total number of active fibers
N_a^{eff}	number of effective active fibers
N_{cr}	critical fiber number at percolation
p	percolation probability
q_{eff}	effective gravimetric capacity with respect to the active material mass
q_{gra}^{eff}	effective gravimetric capacity with respect to the electrode mass
q_{th}	theoretical gravimetric capacity of the active material
q_{vol}^{eff}	effective volumetric capacity with respect to the electrode volume
r	effective ratio
R_c	contact resistance
R_f	fiber resistance
V	volume of the whole electrode
V_a	volume of active fibers
V_a^{eff}	volume of effective active fibers
V_c	volume of conductive fibers
V_e	volume of the electrolyte

conductive fiber content and the active material utilization. The combination of active and conductive materials in fiber form was proposed by Liu et al. [18] for structural battery applications. This novel design, although not fully realized in their experiments, has provided a new direction for the development of multi-functional fiber-based electrodes and will be investigated in Section 3.

In traditional lithium-ion battery electrodes, active material particles act as lithium sources/reservoirs and their amount determines the nominal electrode capacity. Conductive material additives provide pathways for electron transport between current collectors and active material particles, while the electrolyte is where ionic transport takes place. Lithium ions and electrons should meet at the active material-electrolyte interface to allow lithium insertion into the active material [19]. If the supply of ions and electrons is limited, the active material is not fully utilized [9,20–22], and the actual electrode capacity is less than the theoretical value [13,21,23–25]. Experimental evidence [23–25] indicates that the optimization of the weight/volume ratio between active and conductive materials is a key ingredient toward improved electrode capacity and rate capability. Qualitative analogies between particle-based and fiber-based electrodes are expected, but indications regarding the quantitative contributions of the various components in a fiber-based electrode architecture are not yet available. This hinders the investigation of innovative electrode designs that could for instance enable full utilization of the available active material.

Various models have been employed to simulate electrochemical processes in particle-based electrodes and predict the battery response. The pseudo two-dimensional model first proposed by Newman and co-workers [26] describes a porous electrode as a homogenized macroscopic continuum and makes use of a simplified representation of the microstructure for the evaluation of local fields. Although computationally efficient, this approach cannot be applied to fiber-based electrodes if investigations concerning the effect of fiber spatial arrangements are targeted. Full-scale simulations, performed either on entire electrodes [4] or on representative volume elements [22], directly resolve the particle/pore microstructure. However, the discretization of the microstructure of fiber-based electrodes would require a significant computational effort, especially in a parametric study. These models are therefore deemed unsuitable for fiber-based electrode architectures, and a simpler yet effective computational approach is employed in Section 2. The two-step approach that we have devised consists in 1) the determination of the conductive fiber content (percolation threshold, Section 2.1) that ensures the existence of an electronically conductive network, and 2) the identification of the active material fibers accessible to electrons as those in contact with the electronically conductive network (Section 2.3). This approach enables us to explore a wide range of electrode compositions and fiber arrangements in a three-dimensional setting at a relatively low computational cost and to estimate electrode properties such as electronic conductivity, active material utilization, and volumetric/gravimetric capacity. Since we do not simulate electrochemical processes through the solution of governing differential equations, dynamic processes such as ionic transport, solid-state diffusion, and lithiation/delithiation reaction are not part of our evaluations. As these processes are known to affect electrode performance, especially at high charging/discharging rates, our predictions should be considered as a baseline for electrode design.

In Section 3.1, we first describe the methodology to determine the (optimal) active-conductive material ratio that maximizes the gravimetric and volumetric capacities for a given electrode porosity. We then investigate the dependence of the optimal active-conductive ratio on the electrode porosity for different fiber aspect ratios and determine the corresponding gravimetric and

volumetric capacities. The results in Section 3.1.3 indicate a good qualitative agreement with respect to experimental studies on particle-based battery electrodes in terms of active material utilization, gravimetric capacity [23,24], and optimal ratio [25], thus confirming the appropriateness of our modeling assumptions and hypotheses listed at the beginning of Section 2.

The impact of fiber orientation constraints on electronic conductivity (determined through the equivalent resistor network described in Section 2.2) and active material utilization is discussed in Section 3.2 for several conductive fiber contents. We then provide practical guidelines for the arrangement of fibers in electrodes produced, *e.g*, by electrospinning.

2. Computational model and methods

The fiber-based battery electrode under investigation is composed of conductive fibers and active fibers dispersed in a matrix representing the electrolyte. Active fibers are responsible for lithium storage, and their volume fraction determines the nominal capacity of the electrode. Conductive fibers act as electronic conductivity enhancers, analogous to carbon black particles in classical porous battery electrodes. The following main assumptions have been made:

1. The electrolyte is the medium that keeps fibers into place and, although not explicitly modeled, is associated to a volume comprising that of the binder as well;
2. The electrolyte is a perfect electronic insulator;
3. The electronic conduction is exclusively due to the conductive fibers since the electronic conductivity of active materials can be considered negligible (being several orders of magnitude lower than that of conductive materials [3,21,23–25]);
4. All the active fibers in the electrode are assumed to be accessible to ions from the surrounding electrolyte; and
5. The effective electrode capacity is exclusively determined by the active fibers that are in contact with the electronically conductive network formed by the conductive fibers.

Multiple experimental studies have reported electrospun active material nanofibers with a pure structure [14–17]. In these studies, battery electrodes are prepared by mixing active fibers with an electronic conductivity enhancer (Super P). Assumption 3 provides a reasonable approximation of real situations when the active material is characterized by poor electronic conduction. This is the case of lithium manganese oxide ($LiMn_2O_4$), the active material selected as the reference for validation purpose in Section 3.1.3.

As electrochemical processes are not directly simulated, we focus on electrodes undergoing charge/discharge processes at low rates, which permit us to assume that active fibers are always accessible to lithium ions from the surrounding electrolyte. Aspects like solid-state diffusion in the active material and ionic transport in the electrolyte are unlikely to limit the electrode capacity under these conditions, and lithium insertion (extraction) into (from) active fibers is subordinate to the existence of a conduction path for electrons. These circumstances, *per se* relevant to many practical applications, identify the upper bound of the effective electrode capacity at higher rates and thus represent an unavoidable step in electrode design.

In general, the difference between theoretical and actual electrode capacity depends on electronic and ionic pathways within the composite electrode. The optimization of these pathways through the control of electrode composition and structure has been the subject of several studies [9,21,22] that also discussed the existence of a trade-off between electronic and ionic conductivities. The former is enhanced with closely packed electrode structures (low porosity), while the latter is enhanced when the electrolyte has easy access to the composite porous structure (high porosity). In order to ensure the generality of the results without an explicit evaluation of the ionic transport process in the electrolyte, Section 3 discusses how to determine the optimal active-conductive content and the upper bound of the capacity when the electrode porosities are between 0.1 and 0.9.

Experimental evidence indicates that electrospun fibers can overlap: Aravindan et al. [15] and Jayaraman et al. [16,17] have experimentally detected interconnected nanofibers in electrospun fiber mats for electrode applications; Self et al. [13] showed that fiber interconnection can result from fiber ensemble compaction. As the number and spatial distribution of fiber overlaps depend on manufacturing conditions [27], a reliable quantification of the connection density and distribution can only be obtained by means of dedicated experimental investigations, which fall beyond the scope the current study. From the modeling point of view, it has been shown that the estimation of the percolation threshold for soft-shell fibers with hard core depends on the thickness of the soft-shell layer [28]. To limit the number of variables and reduce the computational burden, we generate interconnected fiber networks relying on the soft-core assumption, in agreement with previous studies [29,30]. In this numerical study, conductive and active fibers are inserted into the simulation box by means of the random sequential adsorption algorithm (RSA) [31] according to specific constraints discussed next. Because of the soft-core assumption, fibers can overlap, and the position of a newly generated fiber does not depend on the positions of previously generated fibers.

A unit cubic simulation box with faces parallel to the coordinate planes is considered as a representative volume element of the composite electrode. Each fiber in the electrode is idealized as a spherocylinder of length l and diameter d, with aspect ratio l/d (Fig. 1a); its position is identified through the middle point coordinates and the orientation angle values. Fiber middle points O are assumed to be uniformly distributed, and their coordinates are defined by three independent random numbers from the standard uniform distribution. The two orientation angles are the polar angle θ with respect to the x axis and the azimuthal angle φ with respect to the y axis. We choose the azimuthal angle φ from a uniform distribution over the interval $[0°, 360°]$. As for the polar angle θ, we have considered two cases:

- case I: θ from $0°$ to the limit angle θ_m; and
- case II: θ from the limit angle θ_m to $90°$.

In both cases, limit values are included, and θ_m takes on a value between $0°$ and $90°$. Specific details on the determination of the angle θ can be found in Appendix A. The angle θ_m in case I indicates the degree of fiber alignment along the x direction [32]: when $\theta_m = 90°$, the fibers are isotropically distributed in three dimensions (scenario A); when $\theta_m = 0°$ the fibers are aligned along the x direction (scenario B). In case II, the angle θ_m is related to the degree of fiber alignment on planes perpendicular to the x direction: when $\theta_m = 0°$, the three-dimensional isotropic state (scenario A) is recovered; when $\theta_m = 90°$, the fibers are isotropically distributed over planes parallel to the yoz plane (scenario C). For the three-dimensional isotropic fiber distribution (scenario A), the values of the polar angle θ are such that the fiber end points P (Fig. 1a) uniformly cover the surface of a sphere [29]. Likewise, for the fiber distributions in cases I and II, the polar angles θ are generated in such a way that every differential area on the restricted (by θ_m) sphere surface has the same probability of being a fiber end point. Fibers intersecting the box boundaries are dealt with using the periodicity assumption [33].

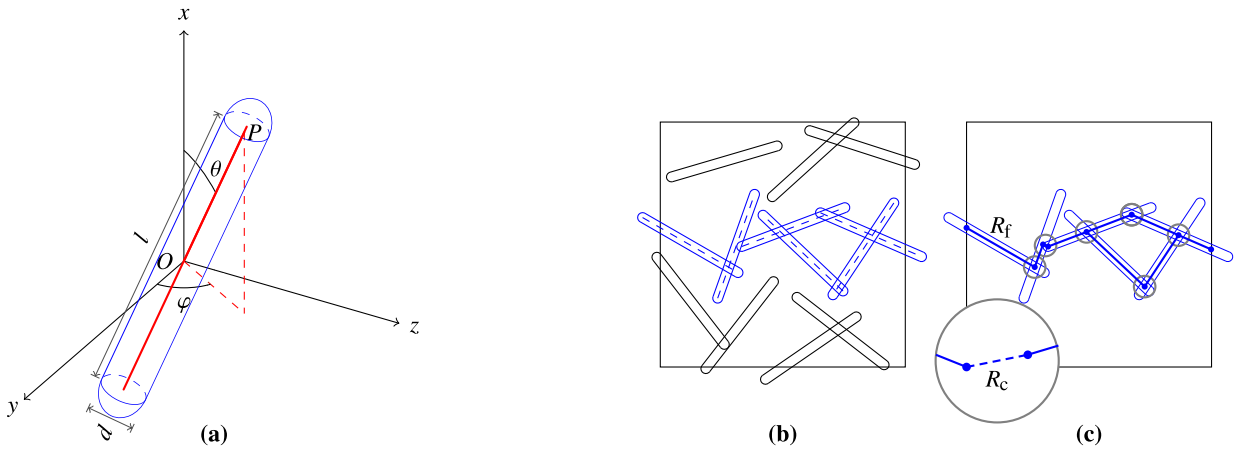

Fig. 1. (a) For each three-dimensional spherocylinder fiber of length l and diameter d in the composite electrode, a spherical coordinate system is attached to its middle point O, and one of its end points (P) is uniquely determined by the two orientation angles θ and φ; the red line indicates the fiber axis. A percolated conductive fiber network (b) is converted into an equivalent resistor network (c) with R_f the resistance of fiber segments and R_c the contact resistance of two connected fiber segments.

The isotropic fiber distribution (scenario A) serves as the reference distribution in Section 3.2 where we study the effect of fiber orientation. Fibers aligned along one direction (scenario B) are known to maximize material properties in that direction (for example, the electronic conductivity in two- [34] and three- [32] dimensional settings). This fiber distribution can be obtained by electrospinning [27]. The planar fiber distribution (scenario C) simulates the layer-like arrangement of electrospun fibers deposited on a substrate [27]; this configuration is of particular interest in this context as layer-by-layer stacked fibers are fabricated to serve as battery electrodes [11,12,27]. Since the battery cell is assembled in such a way that transport processes occur (in average) along the direction perpendicular to the fiber deposition plane, special emphasis is given in Section 3.2 to the description of effective electronic conductivity and capacity in the out-of-plane direction.

A fiber-based electrode consists of three components: active fibers, conductive fibers, and the electrolyte filling the volume surrounding the fibers. We assume that all fibers of a certain type (active or conductive) have the same size. The three components occupy volumes V_a, V_c, and V_e, respectively, and they are related through the relation

$$V_a + V_c + V_e \simeq V, \tag{1}$$

where V is the volume of the entire electrode. Equation (1) is an approximation that does not account for the volume shared by interconnected fibers due to the soft-core assumption. Since the interconnected volume is negligibly small compared to the total fiber volume [29], the error introduced by this assumption is ignored in the following derivations. Dividing Eq. (1) by the electrode volume V yields the relation

$$\phi_a + \phi_c + \phi_e = 1 \tag{2}$$

between the volume fraction of each component where

$$\phi_a = \frac{V_a}{V}, \quad \phi_c = \frac{V_c}{V}, \quad \text{and} \quad \phi_e = \frac{V_e}{V}$$

represent the volume fraction of active fibers, conductive fibers, and electrolyte, respectively. It should be noted that the volume fraction ϕ_e is equivalent to the electrode porosity as it accounts for the volume not occupied by fibers. The relation between volume fraction ϕ and fiber number N is approximated as

$$\phi = \frac{N\pi l d^2}{4L^3}, \tag{3}$$

where L is the box edge length.

The effective electronic conductivity of a fiber-based composite (made up by an insulating matrix and conductive fibers) depends on the fiber content. When the fiber content is low, the response of the hosting matrix prevails and the composite behaves like an insulator; when the fiber content is sufficiently high, the composite behaves as an electronic conductor. The fiber content at which the insulator-conductor transition occurs is known as percolation threshold or critical fiber volume fraction [35,36]. This threshold corresponds to the first formation of an interconnected fiber network along a specific direction. Since a broad literature (Ref. [28] and references therein) is available on the percolation threshold of fiber-based composites, we avoid reporting similar results. The framework for percolation threshold identification, as required by evaluation of electronic conductivity and electrode capacity, is however summarized next. Conventional Monte Carlo methods (Section 2.1) and an equivalent resistor network model (Section 2.2) are used to calculate percolation threshold and conductivity, respectively, by considering conductive fibers only. In Section 2.3, the two species of fibers are taken into account to evaluate the electrode capacity.

2.1. Monte Carlo approach for percolation threshold estimation

Fiber-like inclusions are widely employed to enhance electronic [37,38] and ionic conductivity [39] of solid polymers. In the fiber-based electrodes considered in this study, conductive fibers ensure a continuous path for the transport of electrons from the current collector to the active material. We employ conventional Monte Carlo methods to determine the minimum amount of conductive fibers that ensures the electrode electronic conductivity, *i.e.*, the percolation threshold ϕ_{cr}. The reliability of the numerical procedures used in this part has been verified by means of a comparison against existing theoretical and numerical solutions [29,40] (these comparisons are omitted for brevity).

We assume electrons travel across connected fibers and ignore electron hopping, also known as tunneling effect [41], between

geometrically separated fibers. Conductive fibers i and j are connected if they satisfy the condition

$$h \leq \frac{d_i + d_j}{2}, \tag{4}$$

where d_α represents the diameter of fiber $\alpha\ (=i,j)$, and h is the shortest distance between their axial line segments. A robust algorithm can be found in Ref. [42] to calculate the shortest distance between two line segments. To determine if an interconnected fiber network exists, the fibers in the box that satisfy condition (4) are grouped into the same cluster. If there exists a cluster extending between two opposite faces of the simulation box (refer to the two-dimensional schematic drawing in Fig. 1b and c), the box is defined as being percolated along the direction perpendicular to those faces. The fiber cluster is then identified as the percolated conductive fiber network.

A widely used method [43] to estimate the percolation threshold is to compute the percolation probability p, namely the likelihood of getting percolated, at different fiber contents [43,44] and is briefly described next. The procedure starts by creating m_A simulation boxes with the same number N of fibers but different spatial arrangements. The percolation condition of each fiber arrangement is evaluated by checking whether a percolated conductive fiber network forms across the box. The count of successfully percolated boxes is denoted as n, and the percolation probability is therefore calculated as $p = n/m_A$. By changing the fiber number N and repeating the procedure, a relation can be established between percolation probability p and fiber number N. The fiber number corresponding to a percolation probability of 0.5 is chosen as the percolation threshold [43,44].

The method described above is however computationally expensive. Ma and Gao [37] proposed a cheaper procedure that consists in inserting the conductive fibers one at a time and, after each insertion, checking whether the box percolates. If a percolated conductive fiber network is identified, the procedure is halted and the corresponding number of fibers is identified as the critical fiber number N_{cr} at percolation. The same procedure is repeated m_B times and the percolation threshold is taken as the mean value of the m_B critical fiber numbers.

Although not shown here, our numerical simulation results indicate that these two methods are equivalent: the fiber number with percolation probability of 0.5 is equal to the average critical fiber number N_{cr}. We therefore identify the percolation threshold using the method proposed by Ma and Gao [37]. With an abuse of notation, we indicate with N_{cr} the average critical fiber number and determine the percolation threshold ϕ_{cr} according to Eq. (3).

2.2. Resistor network model

The effective conductivity of the composite electrode depends on factors such as fiber content, fiber distribution, fiber resistance, and the connection between fibers. Here we use the resistor network model to determine the effective conductivity of the composite. The resistor network model has been widely used to evaluate the effective conductivity of composites based either on fibers [30,34,45] or particles [46–50]. The main advantage of this approach is the high degree of flexibility. The geometry of interest is converted into a system of interconnected nodes creating a resistance network, and the effective conductivity of the system is obtained using Kirchhoff's current conservation law.

The resistor network can represent either synthetic (ensembles of spherocylinder or spherical particles packed to mimic the microstructure of a composite material) or real microstructures. Synthetic microstructures can be obtained from discrete element method [46], collision detection and localization optimization method [47], and Monte Carlo approaches [30,45,49,50], while real microstructures can be obtained from focused ion beam-scanning electron microscope images [48,50]. Different strategies can be adopted to convert the microstructure into a resistor network. The simplest way to convert fiber and particle ensembles into resistor networks is to generate nodes at fiber contact points [30,34,45] and particle center points [46,47], respectively. A more elaborate strategy was proposed by Rhazaoui et al. [48] where the geometry is discretized into cubic elements called voxels and the center points of the voxels are converted into nodes of the resistor network. This strategy enabled Rhazaoui et al. [49,50] to convert real electrode microstructure of a solid oxide fuel cell into a resistor network, and to successfully validate the approach by comparing the predicted effective electronic conductivity of the network against experimental data.

Rhazaoui et al. [49] compared the effective conductivity predicted by the resistor network model and the finite element method (solving Laplace's equation) for several geometries. The authors showed that the two methods converge to the same solution irrespective of the geometry, but a higher discretization resolution is required for the resistor network model to ensure a level of accuracy comparable to that of the finite element method. Nevertheless, the drawbacks of the voxelation step in the resistor network approach become apparent when complex geometries (*e.g.*, sintered electrode particles) are simulated [49]. This is not the case when dealing with fiber ensembles, as the fiber segments are directly converted into equivalent resistors connecting nodes (contact points between fibers). The equivalent resistor network is indeed a suitable technique for the evaluation of effective properties of fiber ensembles, especially for fibers of high aspect ratio, as demonstrated in several recent studies [30,32,34,45].

We construct the equivalent resistor network by generating junction nodes from the percolated conductive fiber network, as illustrated in Fig. 1b and c. For each pair of connected fibers, the two closest points on the respective axial line segments are converted into two nodes, and a contact resistor element is added between them. Each fiber segment between two adjacent nodes is transformed into a fiber resistor element. Intersection points between fibers and boundary surfaces of the simulation box are also converted into nodes. Fibers that do not belong to the percolated cluster are disregarded in this process.

For a given simulation box, the effective conductivity along a coordinate axis direction is determined by applying an electric potential difference ΔU between the two opposite box faces perpendicular to that direction and evaluating the corresponding current I_{eff} flowing through the box. The simulation box is considered as a resistor network with each resistor representing either a fiber resistance R_f or a contact resistance R_c between two fibers. The resistance of a fiber segment is proportional to its length via $R_f = \varrho l/S$, where ϱ is the resistivity of the conductive fibers, and l and S are the fiber segment length and cross-sectional area, respectively. In agreement with previous studies [30,45], a unique value is used for the contact resistance R_c.

Applying Ohm's law to each resistor element, we can assemble a system of equations for all the elements [45] and solve for the current flowing through each resistor. The total electrical current I_{eff} is determined by summing up the currents in the resistors. The effective conductivity of the simulation box is calculated as

$$\sigma_{eff} = \frac{I_{eff} L}{\Delta U A}, \tag{5}$$

where A is the cross-sectional area of the box. A thorough verification of the computational tools implemented for this study was

performed by comparing our predictions in term of percolation threshold and electronic conductivity against the data sets reported in Refs. [29,36,40]. Since a good agreement was found, the results are not reported for brevity.

The adoption of a numerical approach ensures a high degree of versatility; this versatility applies not only to the percolation threshold determination but also to the determination of electronic conductivity. In Section 3.2 we evaluate the impact of fiber orientation on the electronic conductivity of the fiber ensemble and extend the two-dimensional results reported by Jagota and Tansu [34] to a three-dimensional setting. In particular, we simulate fiber arrangements with different degrees of orientation with respect to a reference plane. These configurations are of primary relevance for fiber-based battery electrodes produced by electrospinning, where the reference plane corresponds to the deposition substrate.

2.3. Effective ratio of active material

This section describes how to evaluate the active material utilization and electrode capacity. The active material is the source (or reservoir) of lithium and determines the nominal electrode capacity. The active material is usually not fully exploited [19,20,22] as indicated by the fact that the experimentally determined effective gravimetric capacity q_{eff} (expressed per unit mass of active material content) is typically lower than the theoretical gravimetric capacity q_{th} of the active material. For example, for a particle-based $LiMn_2O_4$ cathode, the experimentally determined gravimetric capacity ranges from 120 to 135 mA h g^{-1} at C/24 rate [23,24], while the theoretical (reversible) gravimetric capacity of $LiMn_2O_4$ is approximately 148 mA h g^{-1} [51]. Similar values are reported in Ref. [17] for electrospun $LiMn_2O_4$ nanofibers tested at C/10 rate. These experimental results are affected by factors such as ionic diffusion in the electrolyte, lithium diffusion in the active material, electronic conductivity, and number of charge/discharge cycles. Here we focus on a single limiting factor: the electron's accessibility to active material.

We define as "effective active fibers" the active fibers connected to the percolated conductive fiber network. The actual electrode capacity is exclusively determined by the effective active fibers. We assume that a single contact between an active fiber and the percolated conductive fiber network is enough to make the entire fiber accessible to electrons and available for lithium storage. With this assumption we determine the electrode capacity upper bound. The connection criterion between an active fiber and a conductive fiber is defined as that between conductive fibers in Eq. (4). The total electrode effective capacity

$$C = q_{\text{th}}\, \rho_{\text{a}}\, V_{\text{a}}^{\text{eff}} \tag{6}$$

is expressed as a function of the volume $V_{\text{a}}^{\text{eff}}$ occupied by the effective active fibers, the mass density ρ_{a} of the active material, and the theoretical gravimetric capacity q_{th} (mAh g^{-1}) of the active material. The effective gravimetric capacity

$$q_{\text{eff}} = \frac{C}{\rho_{\text{a}}\, V_{\text{a}}} = q_{\text{th}}\, \frac{V_{\text{a}}^{\text{eff}}}{V_{\text{a}}} \tag{7}$$

is usually expressed in terms of unit mass of the electrode active material, being V_{a} the volume of total active material. We can then introduce the effective ratio

$$r = \frac{q_{\text{eff}}}{q_{\text{th}}} = \frac{V_{\text{a}}^{\text{eff}}}{V_{\text{a}}} \tag{8}$$

that ranges from 0 to 1 by definition.

The effective gravimetric capacity q_{eff} is equivalent to the equilibrium discharge capacity Q_0 identified by Fongy et al. [9,21] and determined from experimental discharge tests performed at low rates (down to C/50 rate). Fongy et al. [21] also calculated the fraction $f_{\text{AMw}} = Q_0/Q_{\text{theoretical}}$ (where $Q_{\text{theoretical}}$ is the theoretical specific capacity of the active material, here denoted with q_{th}) to quantify the active material grains "that are truly electrochemically active", *i.e.*, connected to both electronic and ionic pathways of the composite electrode. Since we are assuming that all active fibers are accessible to ions, the effective ratio r is equivalent to f_{AMw}. The approach adopted here is conceptually reversed compared to that described in Ref. [21], as we move from the (numerically generated) microstructure to estimate the active material utilization through r and we evaluate the electrode capacity afterwards (Section 3.1.2).

Instead of modeling the entire fiber-based electrode, we focus on its response at the material level by studying a cubic simulation box (refer to Section 3). Since all active fibers in the box have the same size, the effective ratio can be expressed as

$$r = \frac{N_{\text{a}}^{\text{eff}}}{N_{\text{a}}}\,, \tag{9}$$

where $N_{\text{a}}^{\text{eff}}$ is the number of effective active fibers and N_{a} is the total number of active fibers.

Due to the soft-core assumption, fibers can overlap and intersect without restrictions. It follows that existing fibers have no influence on the placement of a new fiber. We can thus safely split the procedure for the effective ratio evaluation into two independent steps. First, we generate a simulation box with N conductive fibers and we identify the percolated conductive fiber network. Second, we generate n_{a} configurations by augmenting the conductive fiber configuration of the first step with N_{a} active fibers. The number $N_{\text{a}}^{\text{eff}}$ of active fibers connected to the percolated conductive fiber network is determined in each simulation (the algorithm used to detect contact between fibers is the same as that used in the percolation threshold identification procedure). The effective ratio is calculated according to Eq. (9) for each of the n_{a} configurations. The average of the n_{a} effective ratios is taken as the effective ratio of the conductive fiber configuration under consideration. We observe that the value $N_{\text{a}}^{\text{eff}}$ (and thus r) converges for a "sufficiently large" number of trials. Since the soft-core assumption enables us to generate configurations of active and conductive fibers independently, the number of trials can be increased either by fixing N_{a} and increasing the number of configurations n_{a}, or by fixing n_{a} while increasing the number of active fibers N_{a}. Both strategies, described in Appendix B, have been implemented leading to the same results. We can thus conclude that, due to the soft-core assumption, each active fiber has the same probability of getting connected to the percolated conductive fiber network, if formed. Consequently, the effective ratio only depends on the conductive fiber content and not on the content of the active fibers.

The effective ratio associated with a conductive fiber content of N conductive fibers is determined by repeating the procedure just described for n_{c} configurations of N conductive fibers. The average effective ratio of n_{c} different realizations is taken as the effective ratio for N conductive fibers. When no percolated conductive fiber network exists, a null effective ratio is considered towards the calculation of the average effective ratio. The box number n_{c} is

identified when the average and deviation of n_c effective ratios tend to stabilize as n_c increases. By changing the number of conductive fibers, we repeat the procedure described above to correlate the effective ratio to the number N of conductive fibers. The same procedure is used to identify the number of configurations n_c required to obtain a statistically meaningful value of the electronic conductivity corresponding to the fiber content N.

3. Results and discussions

Carbon nanofibers with high electronic conductivity can be synthesized with diameter in the 100–200 nm range, length in the 5–20 μm range, and aspect ratio in the 10–500 range [9,52]. Electrospun active fibers can be produced with an average diameter that ranges from roughly 1 μm [1] down to 50–100 nm [14], with an average length that varies from a few centimeters down to a few micrometers [15–17], and with aspect ratio that goes from 5 to 20 [15–17] up to extremely large values. In our simulation, active and conductive fibers have diameter $d = 100$ nm and length $l = 2.4$ μm. These values, consistent with those of the fibers produced by Showa Denko [52], have been chosen to obtain fibers with aspect ratio $l/d = 24$, which is the value reported in Ref. [37]. A simulation box with edge length $L = 10$ μm has been employed. This box size yields results that are representative of the electrode's bulk properties, as it is three to twenty times smaller than the characteristic size of the electrodes usually reported in the literature (*e.g.,* Refs. [9,10,21,53]). Nevertheless, this box size is large enough for obtaining meaningful numerical results as it is about five times (*cf.* four to six times in Ref. [54]) larger than the fiber length. This box size ensures a good balance between accuracy and computational cost. By repeating the simulations with several values of L (up to 40 μm), we determined the theoretical percolation threshold (for $L \to \infty$) according to Ref. [35]. The difference between the theoretical value and the percolation threshold obtained with $L = 10$ μm was 5%.

For convenience, the edge length of the simulation box is set to one unit, and the fibers are therefore scaled with respect to the box size: fiber length is $l = 0.24$ units and fiber diameter $d = 0.01$ units. For conciseness of notation, we will omit "unit" when referring to these quantities. Box size and fiber diameter values will not change in the following apart for the discussion on aspect ratio effects (Figs. 2, 4 and 5). Since we are interested in average trends, we report average values of effective ratio, conductivity, and percolation threshold.

Next, we evaluate the active material utilization and the electrode capacity for isotropic fiber distributions (Section 3.1). Section 3.2 is dedicated to study the effect of fiber orientation on percolation threshold, effective conductivity, and effective ratio. The dependence of the active material utilization on the percolation threshold becomes evident when the results of Section 3.1 are used as a reference to study the effect of fiber orientation on the effective ratio.

3.1. Effective active material and capacity

In this section, the interaction between active and conductive fibers will be studied for the evaluation of the electrode capacity. To this end, we start with results related to the utilization of the active material (effective ratio of active fibers), followed by qualitative validations of the proposed approach and an applicative example.

3.1.1. Effective ratio of active fibers

Figure 2a shows the effective ratio r as functions of the conductive fiber volume fraction for three values of the aspect ratio ($l/d = 12$, 24, and 48) together with the percolation probability p for $l/d = 24$. The percolation probability curve is steeper than the effective ratio curve and it divides the diagram into two regions: below the percolation threshold (*e.g.*, for $\phi_c < \phi_{cr} = 0.029$ at $l/d = 24$ in Fig. 2a) the effective ratio is zero because of the absence of a percolated conductive fiber network; above the percolation threshold, the effective ratio increases sharply with the conductive fiber volume fraction. Here the effective ratio is computed as the average value of $n_c = 100$ different conductive fiber configurations, and for each configuration more than $N_a = 10,000$ active fibers are used (refer to Appendix B for details).

It is well known that the percolation threshold depends on the aspect ratio [29]. In a similar manner, the aspect ratio affects the effective ratio in Fig. 2a. Here the aspect ratio l/d is changed by varying the fiber diameter d while keeping the fiber length l unchanged (active and conductive fibers have the same size). The higher the aspect ratio, the lower the conductive fiber volume fraction around which the sharp increase of effective ratio occurs. This is consistent with the conclusion that a higher aspect ratio leads to a lower percolation threshold [29,36].

The effective ratio is also influenced by the relative size of active and conductive fibers (Fig. 2b). This is demonstrated by 1) changing the lengths of all active fibers ($l_a = 2\,l_c$ and $l_a = 0.5\,l_c$) while keeping their diameters fixed, and 2) changing the diameters of all active fibers ($d_a = 1.5\,d_c$ and $d_a = 0.5\,d_c$) while keeping their lengths fixed, where the subscripts a and c indicate active and conductive fibers, respectively. The four cases are compared with the reference case in which active and conductive fibers have the same length and diameter. It is found that the larger (either in length and diameter) the active fiber, the higher the effective ratio. In other words, for a given conductive fiber volume fraction, bigger active fibers should be preferred to increase the effective ratio and, consequently, the electrode capacity (this is mainly due to an increased probability of getting in contact with the percolation network for bigger fibers).

These predictions seem to contrast with the usually observed electrode performance enhancement associated with characteristic dimension reduction of active materials [1,2]. The reason is that the appropriateness of our conclusions is subordinate to the validity of the soft-core assumption and to the suitability of the criteria for discerning if the active fibers are effective or not (the active fiber-conductive fiber network connection is discussed in Section 2.3). In particular, our predictions are appropriate for electrodes composed by nanofibers undergoing quasi-static charge/discharge processes. Under these conditions, solid-state diffusion in the active fibers does not limit the active material utilization, and the fiber diameter can be increased to some extent (the largest fiber radius considered is in the order of hundreds of nanometers). Lithium insertion/extraction into/from active fibers is thus guaranteed if they are accessible to electrons.

When active and conductive fibers have the same size, the inset curves in Fig. 2a suggest the power law relation

$$r = 1 - a\phi_c^b, \tag{10}$$

when $\phi_c > \phi_{cr}$. The average relative error between the data and the fitted values through Eq. (10) is around 1% for all the three aspect ratios (considering all data points). When active and conductive fibers have different lengths or diameters (Fig. 2b), the power law relation fails to fit the effective ratio curve with an average relative error higher than 10%. The error mainly originates from the wide discrepancy between the fitted values and simulated results at conductive fiber volume fractions slightly above the percolation threshold.

3.1.2. Volumetric and gravimetric capacities

Next, we determine the optimal carbon fiber content over a

wide range of electrode porosity. To this end, we evaluate the capacity of the electrode for an assigned electrolyte volume fraction ϕ_e and identify the optimal active-conductive material ratio. Then we repeat the evaluation for ϕ_e in the range $[0.1,\ 0.9]$. The constraint on the volume available for the electrolyte leads to a fixed total volume fraction of the two fiber species,

$$\phi_t = \phi_a + \phi_c = 1 - \phi_e, \tag{11}$$

which takes a value between 0.1 and 0.9.

The expression of the effective capacity in Eq. (7) takes into account only the mass of the active material, neglecting battery components such as polymer binders, electronic conductivity enhancers, and electrolyte. Nevertheless, inactive materials contribute to the overall electrode performance in terms of mass, volume, and overall electrochemical response [20,23,25]. For this reason, it seems appropriate to express the electrode effective capacity (6) per unit volume or mass of the entire electrode to define effective volumetric capacity

$$q_{vol}^{eff} = \frac{C}{V} = q_{th}\,\rho_a\,\phi_a^{eff} = q_{th}\,\rho_a\,(\phi_t - \phi_c)\,r \tag{12}$$

and effective gravimetric capacity

$$q_{gra}^{eff} = \frac{C}{\rho_a V_a + \rho_c V_c + \rho_e V_e} = \frac{q_{th}\,\rho_a\,(\phi_t - \phi_c)\,r}{\rho_e + (\rho_a - \rho_e)\,\phi_t - (\rho_a - \rho_c)\,\phi_c}, \tag{13}$$

where $\rho_a V_a + \rho_c V_c + \rho_e V_e$ is the total electrode mass (*i.e.*, the sum of mass densities multiplied by the volumes of active material, conductive material, and electrolyte), and

$$\phi_a^{eff} = \frac{V_a^{eff}}{V} = \frac{V_a}{V}\,r = \phi_a\,r = (\phi_t - \phi_c)\,r \tag{14}$$

is the volume fraction of the effective active material, obtained

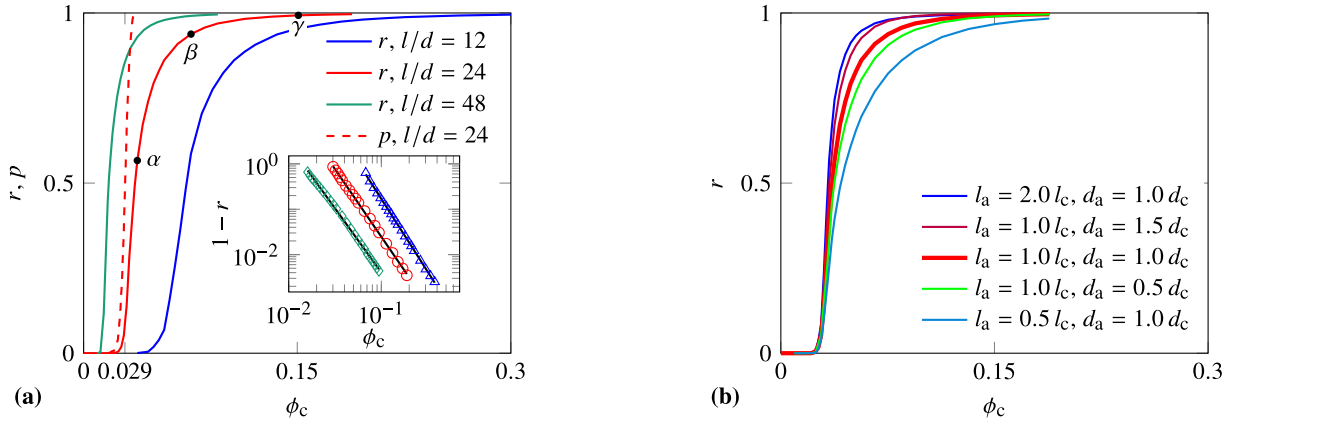

Fig. 2. (a) The main plot shows the effective ratio r versus the conductive fiber volume fraction ϕ_c at three aspect ratios (l/d) and the percolation probability p for $l/d = 24$. The inset graph presents data in a logarithmic scale relating $1 - r$ to ϕ_c (the linear fit indicates a power law relation analogous to Eq. (10) between r and ϕ_c). Conductive and active fibers have the same size at each aspect ratio. Marks α, β, and γ refer to the conductive fiber volume fractions in Fig. 8. (b) Effective ratios r versus conductive fiber volume fraction ϕ_c when active fibers and conductive fibers have different sizes. The length (diameter) of active fibers and conductive fibers are denoted by l_a (d_a) and l_c (d_c), respectively.

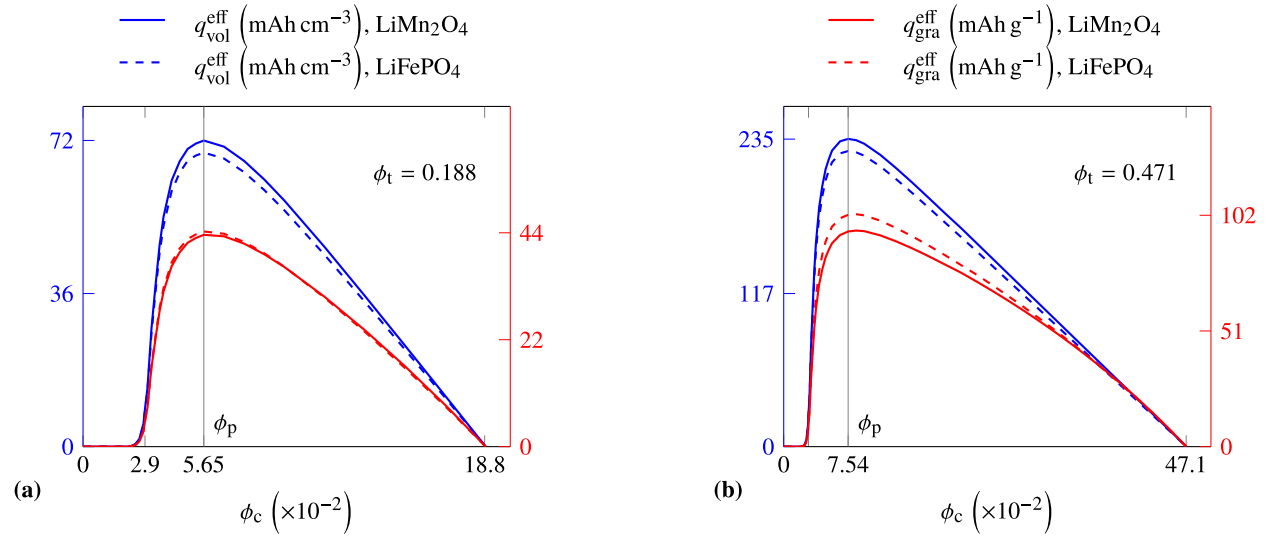

Fig. 3. Volumetric capacity q_{vol}^{eff} (Eq. (12)) and gravimetric capacity q_{gra}^{eff} (Eq. (13)) versus conductive fiber volume fraction ϕ_c at total fiber volume fraction $\phi_t = 0.188$ (a) and 0.471 (b). The optimal conductive fiber volume fraction ϕ_p corresponds to the maximum capacity. The effective ratio r is from Fig. 2a at aspect ratio 24. Solid lines denote $LiMnO_4$, while dashed lines indicates $LiFePO_4$. Material parameters of active materials, conductive materials, and solid polymer electrolyte are listed in Table 1.

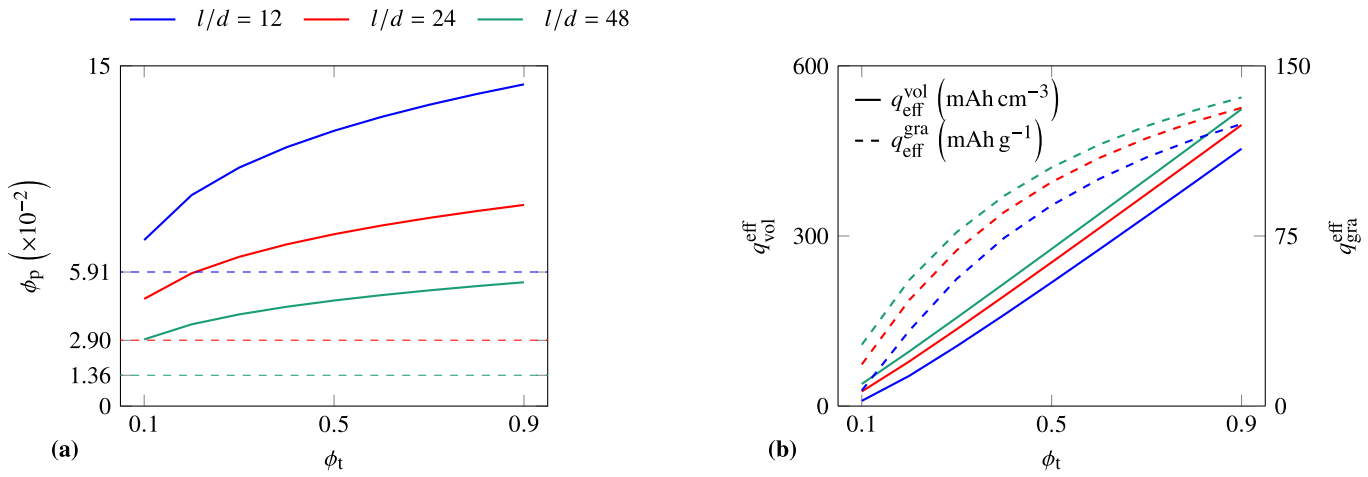

Fig. 4. Optimal conductive fiber volume fraction ϕ_p (a) and volumetric capacity q_{vol}^{eff} and gravimetric capacity q_{gra}^{eff} (b) versus total fiber volume fraction ϕ_t at three different aspect ratios l/d. The dashed horizontal line in (a) denotes the percolation threshold ϕ_{cr}. Material parameters for the active material ($LiMnO_4$), conductive material, and solid polymer electrolyte are listed in Table 1.

considering the definition of its volume from Eq. (8).

Definitions (12) and (13) show that, for a specific set of material properties and a given total fiber content ϕ_t, the volumetric and gravimetric capacities depend on the conductive fiber volume fraction ϕ_c and on the effective ratio r; since r is actually a function of ϕ_c (Fig. 2a), the conductive fiber volume fraction ϕ_c is the only design variable, and these capacities depend on it in a nonlinear fashion. To illustrate the actual dependency, we consider two electrodes that differ in the choice of the active material (we consider active fibers to be made up exclusively by the active material): $LiMn_2O_4$ and lithium iron phosphate ($LiFePO_4$). Despite their poor electronic conductivity [21,23,24,51], which can be addressed with the support of an electronically conductive enhancer, these materials are increasingly popular because of their electrochemical properties, low cost, and reduced toxicity. Moreover, $LiMn_2O_4$ and $LiFePO_4$ nanofibers have been recently produced through electrospinning [15–17,55]. The properties of $LiMn_2O_4$ and $LiFePO_4$, together with those of vapor grown carbon fibers (VGCFs) and the solid polymer electrolyte (SPE), are listed in Table 1.

Figure 3 shows the volumetric and gravimetric capacities for the two active material configurations at two total fiber volume fractions. Since the value of $q_{th}\,\rho_a$ is higher for $LiMnO_4$ than for $LiFePO_4$ (see Table 1), the volumetric capacity q_{vol}^{eff} for $LiMnO_4$ is always higher than that for $LiFePO_4$. The scenario is however different for the gravimetric capacity q_{gra}^{eff}: at $\phi_t = 0.188$, q_{gra}^{eff} is basically the same for $LiMnO_4$ and $LiFePO_4$, while q_{gra}^{eff} for $LiMnO_4$ is lower than that for $LiFePO_4$ at a higher fiber content $\phi_t = 0.471$. These observations indicate that electrode design optimization depends not only on the targeted capacity (q_{vol}^{eff} or q_{gra}^{eff}), but also on the combination of geometrical features and material parameters of both active and inactive components.

The maximum capacity that the composite electrode can achieve (for an assigned ϕ_t) is identified by the peak value of the capacity plot in Fig. 3, and the conductive fiber volume fraction associated with the peak capacity is defined as the optimal conductive fiber volume fraction ϕ_p. This is a relevant quantity to consider in electrode design, in addition to the percolation

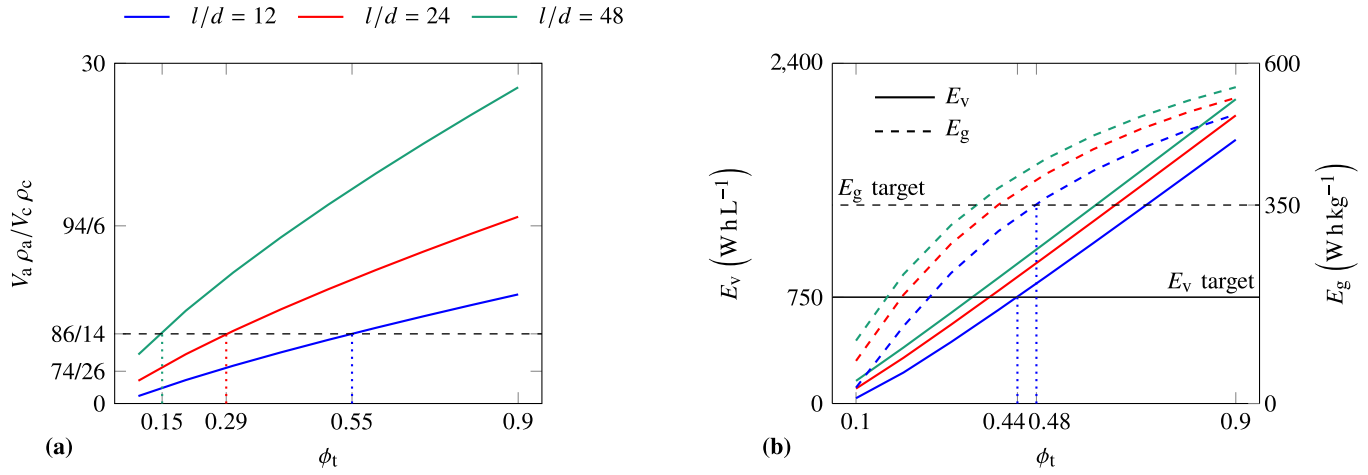

Fig. 5. (a) Active ($LiFePO_4$)-conductive (VGCF) material weight ratio versus total fiber volume fraction ϕ_t at three different aspect ratios l/d. The optimal active-conductive material weight ratio for a particle-based electrode making use of the same active material [25] is indicated by the dashed horizontal line. (b) Volumetric and gravimetric energy densities versus total fiber volume fraction ϕ_t at the three aspect ratios. The two horizontal lines are the energy density targets provided by the European Commission for batteries in automotive applications [58].

Table 1
Material parameters.

Component	Material	Quantity	Reference	Value
active fibers	$LiMn_2O_4$	gravimetric capacity (q_{th})	[23,24]	148.0 mA h g^{-1}
		density (ρ_a)	[23,24]	4.28 g cm^{-3}
	$LiFePO_4$	gravimetric capacity (q_{th})	[56]	169.0 mA h g^{-1}
		density (ρ_a)	[56]	3.6 g cm^{-3}
conductive fibers	VGCF	density (ρ_c)	[52]	2.0 g cm^{-3}
electrolyte	1 M salt, SPE	density (ρ_e)	[57]	1.2 g cm^{-3}

threshold ϕ_{cr}. Figure 3 shows that while ϕ_p differs for different total fiber contents ϕ_t, it is almost the same at a given ϕ_t for q_{vol}^{eff} and q_{gra}^{eff} (the position of the peak differs by 0.6% at most in terms of the capacity) and is independent of the active material considered.

We now study how ϕ_p changes with the total fiber content ϕ_t. Here we focus on cases in which lengths and diameters of active fibers are equal to those of the conductive fibers and consider three aspect ratios ($l/d = 12, 24, 48$). At each aspect ratio, the effective ratio r is approximated by Eq. (10) with the parameters obtained by fitting the corresponding curve in Fig. 2a. Finally, we determine ϕ_p by equating to zero the derivative of expression (12) with respect to ϕ_c. Using this method, we can plot ϕ_p as a function of the total fiber volume fraction as shown in Fig. 4a. As ϕ_t increases, the optimal conductive fiber volume fraction ϕ_p grows and the increase is more drastic at a lower aspect ratio: ϕ_p ranges between 0.07 and 0.14 for $l/d = 12$, between 0.05 and 0.09 for $l/d = 24$, and between 0.03 and 0.05 for $l/d = 48$. The percolation thresholds ϕ_{cr} are also shown here in the same color as ϕ_p. The higher the aspect ratio, the lower ϕ_{cr} and the lower ϕ_p.

Figure 4b shows the capacities q_{vol}^{eff} and q_{gra}^{eff} for $LiMnO_4$ (calculated from Eqs. (12) and (13) at $\phi_c = \phi_p$). We observe that while the volumetric capacity increases with ϕ_t in an approximately linear fashion, the gravimetric capacity rises sharply at low values of ϕ_t and then gently grows with ϕ_t. That is, when the total fiber content is above 0.5 (*i.e.*, the porosity is below 0.5), further electrode compaction leads to a limited gravimetric capacity enhancement. We can also see that at a higher aspect ratio, the capacities q_{vol}^{eff} and q_{gra}^{eff} are higher. Section 3.1.4 completes the discussion of these results.

As a final remark, we stress that the predictions obtained for densely packed fiber ensembles (high total fiber volume fractions ϕ_t) are reported to illustrate the potential of the approach. We are however aware that the soft-core assumption could be questionable above a certain volume fraction threshold, which may lead to a discrepancy between predictions with fully-overlapping fibers and those with non-overlapping fibers. Nevertheless, this volume fraction threshold depends on the property under evaluation [27], and thus the identification of such a threshold value requires a dedicated study.

3.1.3. Comparison with particle-based battery electrodes

Here we provide comparisons between our numerical predictions for fiber-based battery electrodes and experimental data related to particle-based battery electrodes.

Mandal et al. [24] and Lazarraga et al. [23] performed experimental studies on particle-based electrodes using $LiMn_2O_4$ as active material, Super P carbon black (CB) as electronically conductive material, and polyvinylidene fluoride (PVDF) as binder. Electrodes were produced with various proportions of these components. In both studies, the critical carbon black content for percolation was identified from electrical conductivity measurements, and the discharge capacity was evaluated from galvanostatic tests performed at C/24, C/12, and C/5 rates.

Mandal et al. [24, Fig. 8] and Lazarraga et al. [23, Fig. 6] showed that the relationship between the first-cycle discharge capacity (normalized by the weight of the active material) and the carbon black volume fraction follows the same behavior as the effective ratio r in Fig. 2a. This similarity suggests the agreement between our prediction and experimental observation in terms of the dependence of electrode capacity on conductive material; we recall that r quantifies the active material utilization expressed as the ratio of the effective gravimetric capacity of the electrode to the theoretical gravimetric capacity of the active material (Eq. (8)). From a quantitative perspective, Refs. [23,24] reported a percolation threshold $\phi_{CB} \approx 0.03$, and showed that the maximum utilization of the active material was achieved for $\phi_{CB} \geq 0.15$ with the lowest discharge rate (C/24). When considering fibers with aspect ratio 24, we determine a percolation threshold $\phi_{cr} = 0.029$, and full utilization of the active material is achieved for $\phi_c \geq 0.13$ (Fig. 2a). The experimental effective ratio is obtained from Refs. [23,24] by dividing the discharge capacities reported therein by the theoretical gravimetric capacity of $LiMn_2O_4$ (*i.e.*, 148 mA h g^{-1}), according to Eq. (8). If we focus on the maximum active material utilization we observe that $r \approx 0.81$ at most in Ref. [23] (irrespective of the discharge rate), while r attained values between 0.82 and 0.91 when the rate was reduced from C/5 to C/24 in Ref. [24]. The identification of the factors that prevent full electrode utilization ($r < 1$) in the two references falls beyond the scope of this study. However, we attribute the better agreement with Ref. [24], rather than Ref. [23], to the more homogeneous distribution of the components due to the production technique adopted in the former (a detailed discussion about the microstructures obtained in the two references is reported in the latter).

Lazarraga et al. [23] also plotted the first-cycle discharge capacity (normalized by the overall weight of the composite electrode) versus the carbon black content, and they found [23, Fig. 7] a trend analogous to that showed in Fig. 3. The capacity was shown to sharply increase from zero to a finite value at the percolation threshold. A further increase was observed above the percolation threshold up to a maximum (attained at $\phi_{CB} \approx 0.1$), followed by a progressive capacity decrease. Our results (Fig. 3) show a more rapid reduction of the capacity after the peak value when compared with the results reported by Lazarraga et al. [23]. The reason is that the results in Fig. 3 are obtained by applying the constraint (11); however, neither the volume fraction $\phi_{LiMn_2O_4} + \phi_{CB}$ nor the porosity $1 - \phi_{LiMn_2O_4} - \phi_{CB} - \phi_{PVDF}$ were kept constant (the former ranged from 0.37 to 0.64, while the latter ranged from 0.20 to 0.54) in Lazarraga et al. [23], even if the amount of carbon black was progressively increased at the expense of $LiMn_2O_4$. In addition, our theoretical approach enables us to explore electrode compositions up to the limit case $\phi_c = \phi_t$ ($\phi_a = 0$), while the minimum active material volume fraction considered in the reference was $\phi_{LiMn_2O_4} = 0.14$.

Guzmán et al. [25] experimentally investigated the role of active-conductive material weight ratio on the performance (*e.g.*, capacity at different charge/discharge rates and mechanical

integrity) of particle-based electrodes. $LiFePO_4$ and carbon Super P were used as active and conductive materials, respectively. The authors considered active-conductive material weight ratios in the range between 74/26 and 94/6, and they observed that the electrode performance was maximized with the 86/14 ratio. We assume the active material $LiFePO_4$ in fiber form and use VGCFs, in line with the proposed all-fiber computational model. To perform a qualitative comparison between our predictions and the results by Guzmán et al. [25], we employ the active-conductive weight ratio defined as

$$\frac{M_a}{M_c} = \frac{V_a\,\rho_a}{V_c\,\rho_c} = \frac{(\phi_t - \phi_p)\,\rho_a}{\phi_p\,\rho_c}, \tag{15}$$

where ϕ_p is the optimal conductive fiber volume fraction for a given total fiber content ϕ_t as described in Section 3.1, and ρ_a and ρ_c are the densities of the active material $LiFePO_4$ and conductive VGCFs, respectively.

Figure 5a shows the active-conductive material weight ratio, corresponding to the optimal conductive fiber volume fraction in Fig. 4a, as a function of the total fiber content at three fiber aspect ratios (length and diameter are the same for all fibers). The active-conductive weight ratio increases monotonically with ϕ_t and, for increasingly higher aspect ratios, the curves shift upwards and their slopes become steeper. Since the optimal conductive fiber volume fraction depends less and less on the total fiber content when the aspect ratio increases (Fig. 4a), more active fibers can be introduced while the total fiber content increases at a higher aspect ratio. We observe that the active-conductive material weight ratio basically falls in the range of values explored by Guzmán et al. [25] (for particle-based electrodes) when the aspect ratio is equal to 12 and 24, providing a qualitative validation for our results. In addition, the total fiber content corresponding to the intersection between each curve and the optimal active-conductive weight ratio (86/14 according to Guzmán et al. [25]) progressively shifts from 0.15 to 0.55 when the aspect ratio changes from 48 to 12. Roughly speaking, since reduced active-conductive weight ratios are found for reduced aspect ratios, our results suggest that the more the fiber geometry approaches that of a particle, the lower the optimal active-conductive weight ratio becomes. This is in agreement with common design practice of $LiFePO_4$-carbon Super P particle-based electrodes, as they are usually assembled with active-conductive material weight ratio ranging between 80/20 and 86/14 [25].

The good qualitative agreement with experimental results documented in this section suggests that our assumptions are reasonable and our prediction are meaningful, at least for circumstances in which the electrode capacity is controlled by electron transport within the composite (which is clearly the case of the $LiMn_2O_4$-based electrodes considered in Refs. [23,24]).

3.1.4. Practical application

We now show how the tools just described can be used to design fiber-based battery electrodes. To this end, we refer to the guidelines provided by the European Commission for batteries devoted to automotive applications [58]. The target is a battery cell with a volumetric energy density $E_v = 750\ \mathrm{W\,h\,L^{-1}}$ and a gravimetric energy density $E_g = 350\ \mathrm{W\,hkg^{-1}}$. Estimates of the volumetric and gravimetric energy densities can be obtained by multiplying q_{vol}^{eff} and q_{gra}^{eff} (Fig. 4b) by the average electrode potential. With the purpose of providing an illustrative example, we focus on a cell consisting of a $LiMn_2O_4$ fiber-based electrode and a lithium metal counter electrode. We consider an average potential of 4.1 V according to the data reported by Nitta et al. [51]. For simplicity, our evaluation is limited to the contribution of the fiber-based electrode (the contributions of the counter electrode and the separator on the overall cell volume, weight, and capacity should be considered in real applications). Figure 5b shows that in the worst case ($l/d = 12$) the targeted volumetric and gravimetric energy densities are obtained with ϕ_t equal to 0.44 and 0.48, respectively, and thus the higher fiber content satisfies both criteria. The volume fraction that has to be dedicated to the conductive fibers (ϕ_p) is determined from Fig. 4a and it equals 0.12, while the volume fraction occupied by the active fibers in the two configurations is determined from Eq. (11) (0.32 and 0.36, respectively). Figure 5b shows that when the aspect ratio increases, the fiber content that is necessary to meet the targets reduces. Specifically, ϕ_t shifts to 0.34 and 0.36 for the volumetric and gravimetric energy density, respectively, when $l/d = 48$.

3.2. Effect of fiber orientation

This section studies the effect of fiber orientation on percolation threshold, effective conductivity, and effective ratio. We consider the two fiber distribution cases described in Section 2 and report results in the x and y directions. Results in the z direction are the same as those in the y direction because of the uniformly distributed azimuthal angle φ over the interval $[0^\circ, 360^\circ]$ (this is also confirmed by results not reported here).

3.2.1. On percolation threshold

Figure 6 shows the percolation threshold (each point in the plot is the average of 1,000 samples) versus the limit angle θ_m for fiber distribution cases I and II. In both cases, the percolation threshold is lower along the fiber alignment direction (x direction in case I, y direction in case II) than along directions perpendicular to it, irrespective of θ_m.

Figure 6a shows that the percolation thresholds in case I along the x and y directions decrease monotonically with θ_m and eventually converge to the same value, marked by the cross, for the isotropic distribution ($\theta_m = 90^\circ$). For low θ_m values, the conductive fibers are basically aligned along the x direction and parallel to each other. Under these circumstances, a connected fiber network is unlikely to form along either the x or y direction. The maximum percolation threshold along the x direction is achieved at $\theta_m = 0^\circ$ and is three times higher than the isotropic value (0.03); the maximum percolation threshold along the y direction is also achieved at $\theta_m = 0^\circ$ but its actual value has not been determined due to the significant computational burden needed to analyze a single fiber configuration following the procedure in Section 2.1, thus making a statistical analysis unreasonably demanding. The trend of the percolation threshold in the y direction when θ_m approaches 0° is however apparent from Fig. 6a, and the value obtained at $\theta_m = 1^\circ$ is 15 times higher than the corresponding isotropic value.

Although the percolation threshold along the x direction shows a minimum at $\theta_m = 70^\circ$, its value is only 4% lower than the isotropic value. It is therefore safe to conclude that the percolation threshold along the x direction plateaus for $\theta_m > 45^\circ$, without significant loss of accuracy.

In case II (Fig. 6b), the percolation thresholds along the x and y directions start from the isotropic value and increase with θ_m. When $\theta_m = 90^\circ$ (scenario C), all fibers are perpendicular to the x direction and isotropically distributed on planes parallel to the yoz plane. This situation prevents the conductive fibers to form a connected network and thus leads to a percolation threshold increase: the percolation threshold at $\theta_m = 90^\circ$ in the x direction is about two and half times higher than the isotropic value, while a 30% increase is observed along the y direction.

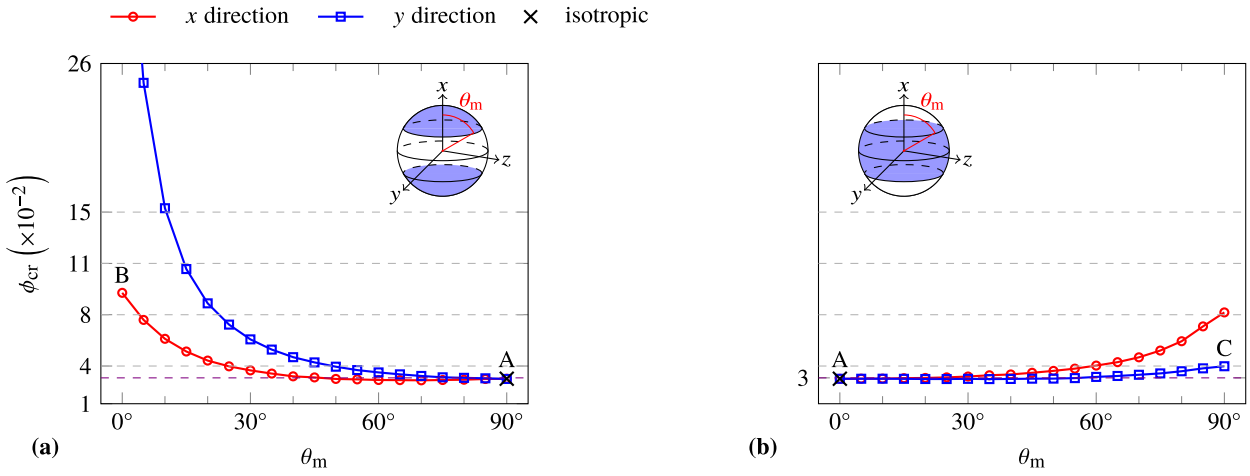

Fig. 6. Percolation threshold ϕ_{cr} versus fiber orientation limit angle θ_m with respect to the x axis for (a) case I ($0° < \theta < \theta_m$) and (b) case II ($\theta_m < \theta < 90°$). The crosses indicate the percolation threshold of the three-dimensional isotropic fiber distribution (the percolation threshold values are the same in both directions and for both cases). Dashed horizontal lines represent the isotropic percolation threshold (0.03) and the four conductive fiber volume fractions (0.04, 0.08, 0.11, 0.15) in Figs. 7 and 8. Points A, B, and C correspond to scenarios A, B, and C in Section 2, respectively.

As expected, the isotropic fiber distribution minimizes the percolation threshold (refer for example to Balberg et al. [59]). However, the percolation threshold variation in case I is more pronounced than that in case II along the x and y directions. A threefold and twofold increase with respect to the isotropic value is observed along the x direction in the two cases, respectively. Furthermore, the percolation threshold increase along the x direction in case II is pronounced from $\theta_m > 40°$ onwards (Fig. 6b). This is relevant to fiber-based electrodes produced by electrospinning. As fibers are deposited on a substrate that can be identified with the *yoz* plane, our results suggest that it is beneficial to introduce some degree of randomness along the out-of-plane direction (x direction) to favor percolation in that direction. This would lead to an increased electronic conductivity (Fig. 7b) and a higher effective ratio (Fig. 8b) through the electrode thickness.

In Fig. 6, the percolation thresholds along the x and y directions coincide when θ_m approaches 90° and 0° in case I and case II, respectively. This confirms that fibers are distributed uniformly and isotropically in the simulation box in these two limit cases, and that they are both representative of the isotropic fiber distribution.

3.2.2. On effective conductivity

Figure 7 shows the effective conductivity against θ_m for case I and case II at three conductive fiber volume fractions (0.08, 0.11, and 0.15). The effective conductivity is defined as the conductivity σ normalized by σ_{iso} (*i.e.*, σ of the three-dimensional isotropic fiber distribution for each conductive fiber volume fraction). Simulations have been performed using $\varrho/S = 1\ \Omega$/unit and $R_c = 1.5\ k\Omega$. It should be kept in mind that the electronic conductivity monotonically increases with the conductive fiber content for isotropic distributions [34].

In Fig. 7a, the conductivities along the x and y directions approach zero at low θ_m values (highly aligned fibers). This is because the percolation thresholds at low θ_m values (Fig. 6a) are higher than the conductive fiber content. As θ_m increases, the conductivity along the x direction increases and shows the existence of a maximum. This indicates that a certain degree of alignment improves the conductivity along the alignment direction (this is for instance beneficial to applications that only require unidirectional conduction [34]). A higher degree of alignment seems to be preferable at a higher conductive fiber content: the higher the fiber volume fraction, the lower the limit angle θ_m to attain the maximum conductivity (θ_m shifts from 55° to 45° as the fiber volume fraction increases from 0.08 to 0.15). Moreover, the conductivity enhancement that can be achieved by aligning fibers along a specific direction is more appreciable at a higher fiber volume fraction, as suggested by the higher normalized conductivity σ/σ_{iso} (whose value increases from 1.55 to 1.70 when the fiber volume fraction increases from 0.08 to 0.15). The conductivity along the y direction increases monotonically with θ_m, and the variation patterns basically coincide for the three volume fractions. As θ_m increases to 90°, the conductivities along both directions converge to the isotropic value. The trends shown in Fig. 7a have been reported in previous studies restricted to two-dimensional fiber arrangements [34,60], thus providing a verification of our numerical framework. Next we extend the investigation by examining the effect of fiber alignment on a plane.

For the second fiber distribution case (Fig. 7b), the conductivities along both directions equal the isotropic value at $\theta_m = 0°$. The conductivity along the y direction mirrors the trend of the conductivity along the x direction for case I in Fig. 7a. However, the peak conductivity ($\sigma/\sigma_{iso} \approx 1.3$) is lower than the peak value in case I for each conductive fiber volume fraction. This suggests that the fiber alignment effect is more pronounced when fibers are aligned along a specific direction (the x direction in case I) than fibers aligned along a random direction on a plane (the y direction is representative of any other direction on the *yoz* plane in case II). We observe that the conductivity along the x direction decreases monotonically with θ_m regardless of the fiber volume fraction. Since the electronic conduction in the electrode thickness direction (the x direction in case II) is crucial to battery rate performance [23,24], these observations suggest that the weaker the constraint on fiber orientation in electrospun fiber-based electrodes, the better the performance.

3.2.3. On effective ratio

Figure 8 shows the influence of fiber orientation on the effective ratio for three conductive fiber volume fractions (0.04, 0.08, and 0.15, denoted by α, β, and γ, respectively, in Fig. 2a). For non-isotropic fiber distributions, the effective ratio along the x

direction is calculated by counting the active fibers connected with the percolated conductive fiber networks along the x direction, while the effective ratio along the y direction is defined as the fraction of the active fibers connected to percolated fiber networks along the y direction. Note that both fibers follow the same distribution in terms of fiber middle points and orientations.

In case I (Fig. 8a), the effective ratio increases monotonically from zero to the isotropic value at $\theta_m = 90^\circ$ for both directions and at each conductive fiber volume fraction. Since the percolation threshold along the x direction is always lower than that along the y direction (Fig. 6a), the percolated fiber network will first form along the x direction as θ_m increases (percolation threshold decreases). The percolated cluster along the x direction is usually different from the one along the y direction and involves more fibers; it follows that the transition starts at a higher θ_m value for the y direction, irrespective of the conductive fiber volume fraction. Above a certain

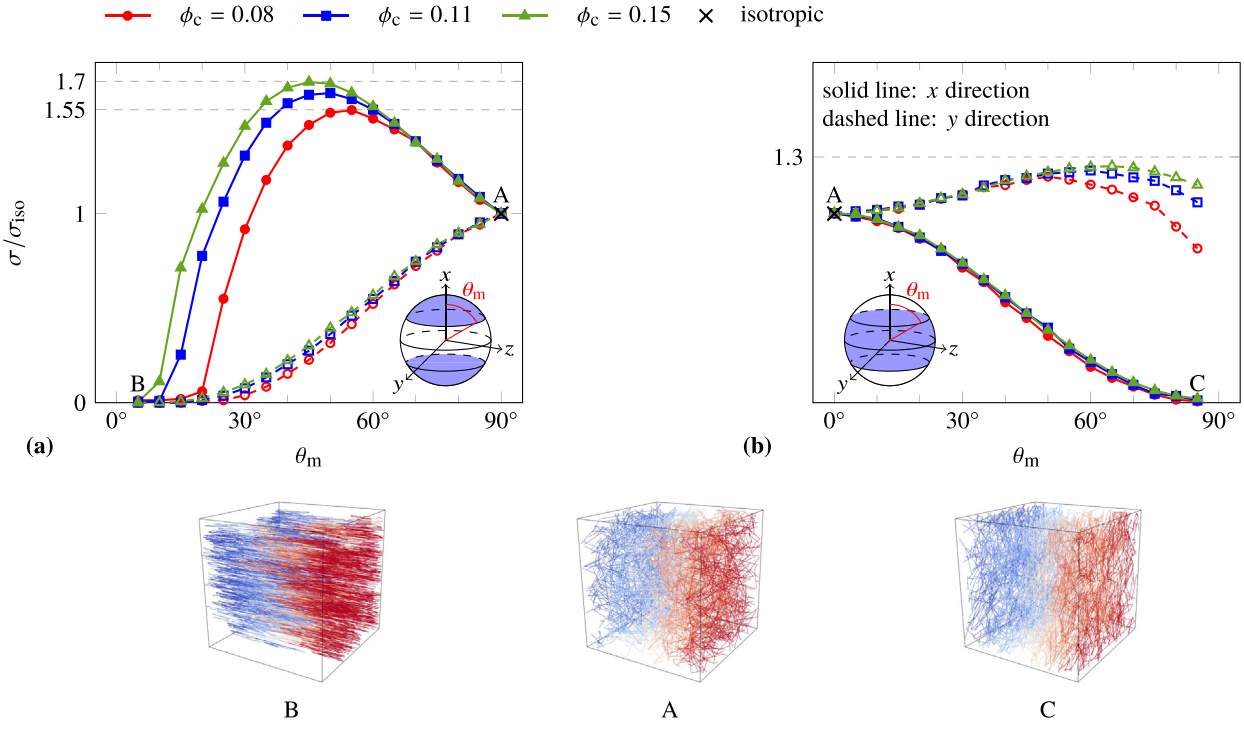

Fig. 7. Conductivity curves normalized by the corresponding isotropic conductivities σ_{iso} versus the fiber orientation limit angle θ_m with respect to the x axis for case I (a) and case II (b) at three different conductive fiber volume fractions ϕ_c. The isotropic conductivity σ_{iso} is the value of σ at $\theta = 90^\circ$ in panel (a) and $\theta = 0^\circ$ in panel (b). Note that σ_{iso} values for the three conductive fiber volume fractions are different. However, the isotropic conductivities σ_{iso} for each conductive fiber volume fraction, in both directions and for both cases, are the same. The bottom subplots show the electric potential distribution of the equivalent resistor network for scenario A (isotropic fiber distribution), scenario B (fibers aligned along the x direction), and scenario C (fibers perpendicular to the x direction) as described in Section 2. The potential of all nodes on the left-hand side surface is set to zero, while an electric potential equal to 1 V is applied to all nodes on the right-hand side surface.

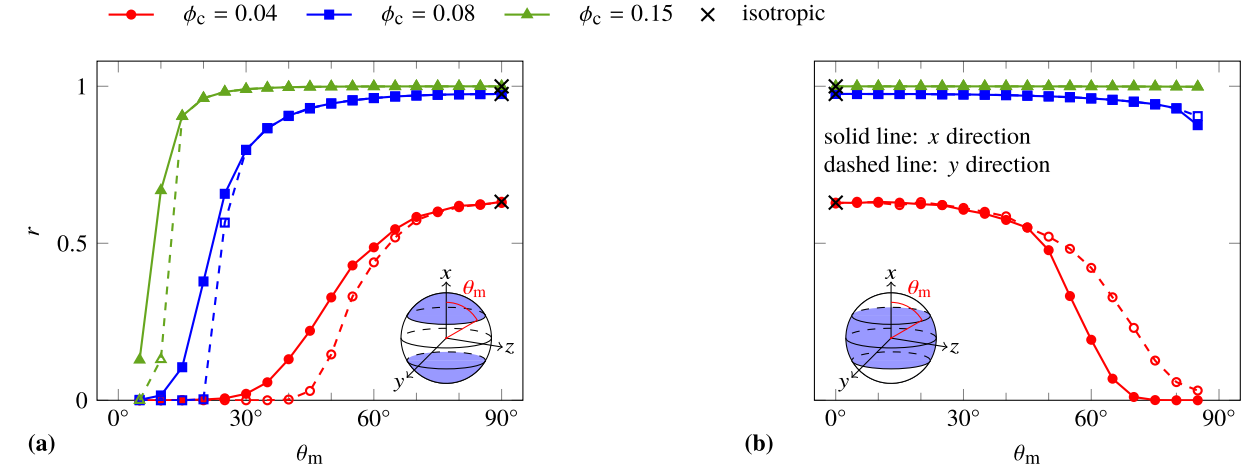

Fig. 8. Effective ratio r in the x and y directions as a function of the fiber orientation limit angle θ_m with respect to the x axis at three different conductive fiber volume fractions ϕ_c for case I (a) and case II (b). The effective ratio values for each conductive fiber volume fraction for the three-dimensional isotropic distribution are the same in both directions and for both cases.

value of the limit angle θ_m, the percolated fiber clusters along the x and y directions merge into a single one, and the curves of the effective ratios overlap. As the conductive fiber volume fraction increases, the transition of the effective ratio occurs at a lower θ_m value both in the x and y directions and it becomes sharper; the overlap between the curves in the x and y directions occurs also earlier.

The arguments just exposed also apply to case II in Fig. 8b, with a few differences. First, the plots in Fig. 8b appear mirrored compared to those in Fig. 8a, with maximum r at $\theta_m = 0^\circ$ (isotropic value). Second, two of the three selected conductive fiber volume fractions are above the percolation threshold curves in Fig. 6b; for this reason the trends of the corresponding effective ratios versus θ_m are also different. Figure 6b shows that the conductive fiber volume fractions 0.08 and 0.15 are higher than the percolation threshold irrespective of θ_m, while the volume fraction 0.04 exceeds the percolation threshold only for a limited interval of θ_m (above $\theta_m = 55^\circ$ in the x direction, and above $\theta_m = 85^\circ$ in the y direction). It follows that the effective ratios shown in Fig. 8b for $\phi_c = 0.08$ and $\phi_c = 0.15$ are basically constant and equal to the isotropic value along both directions (apart from a 10% reduction for $\phi_c = 0.08$ starting from $\theta_m = 50^\circ$), while a transition from the isotropic value ($\theta_m = 0^\circ$) towards a value that approaches zero ($\theta_m = 90^\circ$) is clearly visible for $\phi_c = 0.04$, similar to those observed in Fig. 8a.

Since the fraction of effective active fibers is subordinate to the presence of a percolated conductive fiber network, the impact of fiber orientation on the percolation threshold reflects on the effective ratio. The isotropic fiber distribution minimizes the percolation threshold and maximizes the effective ratio. At a given conductive fiber content, the higher the deviation from an isotropic distribution, the higher the reduction of the effective ratio. However, Fig. 8 shows that the impact of fiber orientation reduces as the conductive fiber content increases. This means that the conductive fiber volume fraction that guarantees full utilization of the active material ($r = 1$, Fig. 2a) also makes the active material utilization insensible to fiber orientation constraints, thus providing a useful information for fiber-based electrode design (being the effective volumetric and gravimetric capacities related to the effective ratio through Eqs. (12) and (13)).

4. Conclusions

The results of this numerical study indicate that volumetric and gravimetric capacities (Fig. 3) are maximized for a particular (optimal) active-conductive material ratio, and the corresponding optimal conductive fiber content is higher than the percolation threshold (Fig. 4). However, an excess of conductive material lowers the capacities, in agreement with experimental studies performed on particle-based electrodes [23,25]. Since the electronic conductivity increases monotonically with the conductive fiber content [34], we conclude that the trade-off between energy and power requirements, that is known to characterize particle-based electrode design, holds also for fiber-based electrodes.

Additionally, the results suggest that geometrical constrains (*e.g.*, fiber orientation) impact on the effective properties. Isotropic fiber distributions lead to the lowest percolation threshold (Fig. 6) and to the highest active material utilization (effective ratio, Fig. 8) for a given conductive fiber content. Nevertheless, this does not apply to the electronic conductivity as its maximum value along a direction is achieved for fibers with moderate angles of fiber misalignment with respect to that direction. We conclude that restrictions on fiber orientation must be considered for the design and optimization of electrodes according to capacity (active material utilization) and power (electronic conductivity) requirements. Fiber orientation therefore represents an additional, compared to particle-based electrodes, degree of freedom in electrode design that can be exploited to strike a balance between electrode capacity and power density. In addition, the isotropic fiber distribution is significantly advantageous to active material utilization only when the conductive fiber content is low, while a limited effect on the active material utilization is observed at higher conductive fiber contents (Fig. 8). This suggests that when constraints on fiber orientation apply, the active material utilization changes more drastically with the conductive fiber content. An interesting design question thus arises for applications where fiber orientation is constrained: can we still identify an optimal active-conductive fiber ratio that maximizes the capacity when the total fiber content is fixed, similar to Fig. 3 for isotropic fiber distribution? These observations are of interest not only for electrospun fiber-based electrodes [2] but also for structural batteries [18], where preferential fiber orientations can be desirable to attain specific mechanical performance.

The approaches and computational tools implemented in this study are rather flexible, and they can be used to handle the more general case of active material fibers with a non-negligible electronic conductivity. In such a case, the electrode conductivity is expected to increase for the same active and conductive fiber contents with respect to our current predictions (this can be ascertained by considering an intrinsic electronic conductivity for the resistors representing active fibers in the resistor network model), and the percolation threshold is expected to depend on the ratio between the electronic conductivities of the two families of fibers. This latter observation implies that percolation threshold and effective ratio become not uniquely defined for an assigned volume fraction of active and conductive fibers, with the consequence that a priori predictions are not possible.

Our computational model can be modified to consider electrodes composed either of conductive fibers and active particles [8–10] or conductive particles and active fibers [14–17]. Further extension are in principle possible. For example, real electrode geometries could be addressed by coupling the model to the procedure proposed by Rhazaoui et al. [48] to convert a realistic electrode microstructure to voxels and voxels to a resistor network.

Acknowledgements

The research leading to these results has received funding from the European Research Council under the European Union's Seventh Framework Programme (FP7/2007–2013) / ERC Grant agreement n° 617972.

Appendix A. Random fiber generation

(1) For a three-dimensional isotropic fiber distribution (scenario A), the polar angle θ is taken as

$$\theta = \cos^{-1}(1 - \text{rand}), \tag{A.1}$$

where rand is a uniformly distributed random number in the interval $[0, 1]$.

(2) For a general fiber distribution in case I (shaded surface on the sphere reported in Fig. 6a), we determine the polar angle θ by solving

$$1 - \cos\theta = (1 - \cos\theta_m)\,\text{rand}, \tag{A.2}$$

where θ_m is between 0° and 90°. When $\theta_m = 90^\circ$, Eq. (A.2) turns into (A.1).

(3) For a general fiber distribution in case II (shaded surface on the sphere reported in Fig. 6b), the equation to solve for θ is

$$1 - \cos\theta = 1 - \cos\theta_m + \cos\theta_m \, \text{rand}, \quad \text{(A.3)}$$

where θ_m is between 0° and 90°. When $\theta_m = 0°$, Eq. (A.3) turns into (A.1).

Appendix B. Effective ratio determination

We claim that the effective ratio is independent of the active fiber content and only depends on the conductive fiber content. This is a consequence of the soft-core assumption: since fibers can overlap, the position of each fiber in the simulation box does not depend on the position of any other fiber. We verify this claim by means of the procedure reported below.

1. We generate a conductive fiber configuration with N fibers.
2. We generate n_a configurations by augmenting the conductive fiber configuration in step 1 with N_a active fibers.
3. The effective ratio for each of the n_a configurations is determined via Eq. (9); r indicates the average value of the n_a effective ratios.
4. We repeat steps 2–3 100 times changing the number N_a of active fibers. We find that, when n_a is high enough (1,000 in our simulations), the average effective ratio values r are the same at different values of N_a. Therefore, for a fixed conductive fiber configuration, the effective ratio does not depend on the number N_a of active fibers.
5. We generate 100 configurations with N conductive fibers and repeat steps 2–4. For all the configurations the effective ratio does not depend on the specific number of active fibers.
6. We further repeat all the previous steps for different numbers N of conductive fibers and obtained the same results.

As an alternative to the above procedure, for each conductive fiber configuration we suggest to use $N_a \geq 10,000$ and $n_a = 1$.

References

[1] W. Li, L. Zeng, Y. Wu, Y. Yu, Nanostructured electrode materials for lithium-ion and sodium-ion batteries via electrospinning, Sci. China Mater. 59 (4) (2016) 287–321, https://doi.org/10.1007/s40843-016-5039-6.

[2] J.-W. Jung, C.-L. Lee, S. Yu, I.-D. Kim, Electrospun nanofibers as a platform for advanced secondary batteries: a comprehensive review, J. Mater. Chem.A 4 (2016) 703–750, https://doi.org/10.1039/C5TA06844D.

[3] B. Zhang, F. Kang, J.-M. Tarascon, J.-K. Kim, Recent advances in electrospun carbon nanofibers and their application in electrochemical energy storage, Prog. Mater. Sci. 76 (2016) 319–380, https://doi.org/10.1016/j.pmatsci.2015.08.002.

[4] W. Mai, M. Yang, S. Soghrati, A particle-resolved 3D finite element model to study the effect of cathode microstructure on the behavior of lithium ion batteries, Electrochim. Acta 294 (2019) 192–209, https://doi.org/10.1016/j.electacta.2018.10.072.

[5] Z. Zhang, F. Xiao, S. Wang, Hierarchically structured MnO_2/graphene/carbon fiber and porous graphene hydrogel wrapped copper wire for fiber-based flexible all-solid-state asymmetric supercapacitors, J. Mater. Chem.A 3 (21) (2015) 11215–11223, https://doi.org/10.1039/c5ta02331a.

[6] Z. Zhang, F. Xiao, J. Xiao, S. Wang, Functionalized carbonaceous fibers for high performance flexible all-solid-state asymmetric supercapacitors, J. Mater. Chem.A 3 (22) (2015) 11817–11823, https://doi.org/10.1039/c5ta01990g.

[7] Z. Zhang, S. Liu, J. Xiao, S. Wang, Fiber-based multifunctional nickel phosphide electrodes for flexible energy conversion and storage, J. Mater. Chem.A 4 (24) (2016) 9691–9699, https://doi.org/10.1039/c6ta03732a.

[8] S. Ahn, Y. Kim, K.J. Kim, T.H. Kim, H. Lee, M.H. Kim, Development of high capacity, high rate lithium ion batteries utilizing metal fiber conductive additives, J. Power Sources 81 (1999) 896–901, https://doi.org/10.1016/S0378-7753(99)00133-0.

[9] C. Fongy, S. Jouanneau, D. Guyomard, B. Lestriez, Carbon nanofibers improve both the electronic and ionic contributions of the electrochemical performance of composite electrodes, J. Power Sources 196 (20) (2011) 8494–8499, https://doi.org/10.1016/j.jpowsour.2011.06.022.

[10] I. Cho, J. Choi, K. Kim, M.-H. Ryou, Y.M. Lee, A comparative investigation of carbon black (Super-P) and vapor-grown carbon fibers (VGCFs) as conductive additives for lithium-ion battery cathodes, RSC Adv. 5 (2015) 95073–95078, https://doi.org/10.1039/C5RA19056H.

[11] B.N. Joshi, S. An, H.S. Jo, K.Y. Song, H.G. Park, S. Hwang, S.S. Al-Deyab, W.Y. Yoon, S.S. Yoon, Flexible, freestanding, and binder-free SnO_x-ZnO/carbon nanofiber composites for lithium ion battery anodes, ACS Appl. Mater. Interfaces 8 (14) (2016) 9446–9453, https://doi.org/10.1021/acsami.6b01093.

[12] E.C. Self, R. Wycisk, P.N. Pintauro, Electrospun titania-based fibers for high areal capacity Li-ion battery anodes, J. Power Sources 282 (2015) 187–193, https://doi.org/10.1016/j.jpowsour.2015.02.036.

[13] E.C. Self, E.C. McRen, R. Wycisk, P.N. Pintauro, $LiCoO_2$-based fiber cathodes for electrospun full cell Li-ion batteries, Electrochim. Acta 214 (2016) 139–146, https://doi.org/10.1016/j.electacta.2016.08.033.

[14] N. Arun, V. Aravindan, S. Jayaraman, N. Shubha, W.C. Ling, S. Ramakrishna, S. Madhavi, Exceptional performance of a high voltage spinel $LiNi_{0.5}Mn_{1.5}O_4$ cathode in all one dimensional architectures with an anatase TiO_2 anode by electrospinning, Nanoscale 6 (2014) 8926–8934, https://doi.org/10.1039/C4NR01892C.

[15] V. Aravindan, J. Sundaramurthy, P.S. Kumar, N. Shubha, W.C. Ling, S. Ramakrishna, S. Madhavi, A novel strategy to construct high performance lithium-ion cells using one dimensional electrospun nanofibers, electrodes and separators, Nanoscale 5 (2013) 10636–10645, https://doi.org/10.1039/C3NR04486F.

[16] S. Jayaraman, V. Aravindan, P. Suresh Kumar, W. Chui Ling, S. Ramakrishna, S. Madhavi, Exceptional performance of $TiNb_2O_7$ anode in all one-dimensional architecture by electrospinning, ACS Appl. Mater. Interfaces 6 (11) (2014) 8660–8666, https://doi.org/10.1021/am501464d.

[17] S. Jayaraman, V. Aravindan, P. Suresh Kumar, W.C. Ling, S. Ramakrishna, S. Madhavi, Synthesis of porous $LiMn_2O_4$ hollow nanofibers by electrospinning with extraordinary lithium storage properties, Chem. Commun. 49 (2013) 6677–6679, https://doi.org/10.1039/C3CC43874K.

[18] P. Liu, E. Sherman, A. Jacobsen, Design and fabrication of multifunctional structural batteries, J. Power Sources 189 (1) (2009) 646–650, https://doi.org/10.1016/j.jpowsour.2008.09.082.

[19] N.J. Dudney, J. Li, Using all energy in a battery, Science 347 (6218) (2015) 131–132, https://doi.org/10.1126/science.aaa2870.

[20] H. Zheng, R. Yang, G. Liu, X. Song, V.S. Battaglia, Cooperation between active material, polymeric binder and conductive carbon additive in lithium ion battery cathode, J. Phys. Chem. C 116 (7) (2012) 4875–4882, https://doi.org/10.1021/jp208428w.

[21] C. Fongy, A.-C. Gaillot, S. Jouanneau, D. Guyomard, B. Lestriez, Ionic vs electronic power limitations and analysis of the fraction of wired grains in $LiFePO_4$ composite electrodes, J. Electrochem. Soc. 157 (7) (2010) A885–A891, https://doi.org/10.1149/1.3432559.

[22] Y.-H. Chen, C.-W. Wang, X. Zhang, A. Sastry, Porous cathode optimization for lithium cells: ionic and electronic conductivity, capacity, and selection of materials, J. Power Sources 195 (9) (2010) 2851–2862, https://doi.org/10.1016/j.jpowsour.2009.11.044.

[23] M.G. Lazarraga, M. Sankar, J. Ibáñez, J.M. Amarilla, J.M. Rojo, $LiMn_2O_4$-based composites processed by a chemical-route: microstructural, electrical, electrochemical, and mechanical characterization, J. Power Sources 115 (2) (2003) 315–322, https://doi.org/10.1016/S0378-7753(03)00011-9.

[24] S. Mandal, J.M. Amarilla, J. Ibáñez, J.M. Rojo, The role of carbon black in $LiMn_2O_4$-based composites as cathodes for rechargeable lithium batteries, J. Electrochem. Soc. 148 (1) (2001) A24–A29, https://doi.org/10.1149/1.1339026.

[25] G. Guzmán, J. Vazquez-Arenas, G. Ramos-Sánchez, M. Bautista-Ramírez, I. González, Improved performance of $LiFePO_4$ cathode for Li-ion batteries through percolation studies, Electrochim. Acta 247 (2017) 451–459, https://doi.org/10.1016/j.electacta.2017.06.172.

[26] M. Doyle, T.F. Fuller, J. Newman, Modeling of Galvanostatic Charge and Discharge of the Lithium/Polymer/Insertion Cell, Journal of The Electrochemical Society 140 (6) (1993) 1526–1533, https://doi.org/10.1149/1.2221597.

[27] J.H. Wendorff, S. Agarwal, A. Greiner, Electrospinning: Materials, Processing, and Applications, 1st ed., John Wiley & Sons, 2012 https://doi.org/10.1002/9783527647705.

[28] L. Berhan, A.M. Sastry, Modeling percolation in high-aspect-ratio fiber systems. I. Soft-core versus hard-core models, Phys. Rev. E 75 (4) (2007), 041120, https://doi.org/10.1103/PhysRevE.75.041120.

[29] M. Foygel, R.D. Morris, D. Anez, S. French, V.L. Sobolev, Theoretical and computational studies of carbon nanotube composites and suspensions: electrical and thermal conductivity, Phys. Rev. B 71 (2005) 104201, https://doi.org/10.1103/PhysRevB.71.104201.

[30] R.M. Mutiso, M.C. Sherrott, A.R. Rathmell, B.J. Wiley, K.I. Winey, Integrating simulations and experiments to predict sheet resistance and optical transmittance in nanowire films for transparent conductors, ACS Nano 7 (9) (2013) 7654–7663, https://doi.org/10.1021/nn403324t.

[31] Y. Pan, L. Iorga, A.A. Pelegri, Analysis of 3D random chopped fiber reinforced composites using FEM and random sequential adsorption, Comput. Mater. Sci. 43 (3) (2008) 450–461, https://doi.org/10.1016/j.commatsci.2007.12.016.

[32] W.S. Bao, S.A. Meguid, Z.H. Zhu, M.J. Meguid, Modeling electrical conductivities of nanocomposites with aligned carbon nanotubes, Nanotechnology 22 (48) (2011) 485704, https://doi.org/10.1088/0957-4484/22/48/485704.

[33] H. Meyer, P. Van der Schoot, T. Schilling, Percolation in suspensions of polydisperse hard rods: quasi universality and finite-size effects, J. Chem. Phys. 143 (4) (2015), 044901, https://doi.org/10.1063/1.4926946.
[34] M. Jagota, N. Tansu, Conductivity of nanowire arrays under random and ordered orientation configurations, Sci. Rep. 5 (2015) 10219, https://doi.org/10.1038/srep10219.
[35] A. Aharony, D. Stauffer, Introduction to Percolation Theory, Taylor & Francis, 2003.
[36] R.M. Mutiso, K.I. Winey, Electrical properties of polymer nanocomposites containing rod-like nanofillers, Prog. Polym. Sci. 40 (2015) 63–84, https://doi.org/10.1016/j.progpolymsci.2014.06.002.
[37] H. Ma, X.-L. Gao, A three-dimensional Monte Carlo model for electrically conductive polymer matrix composites filled with curved fibers, Polymer 49 (19) (2008) 4230–4238, https://doi.org/10.1016/j.polymer.2008.07.034.
[38] W. Bauhofer, J.Z. Kovacs, A review and analysis of electrical percolation in carbon nanotube polymer composites, Compos. Sci. Technol. 69 (10) (2009) 1486–1498, https://doi.org/10.1016/j.compscitech.2008.06.018.
[39] W. Liu, N. Liu, J. Sun, P.-C. Hsu, Y. Li, H.-W. Lee, Y. Cui, Ionic conductivity enhancement of polymer electrolytes with ceramic nanowire fillers, Nano Lett. 15 (4) (2015) 2740–2745, https://doi.org/10.1021/acs.nanolett.5b00600.
[40] S.I. White, R.M. Mutiso, P.M. Vora, D. Jahnke, S. Hsu, J.M. Kikkawa, J. Li, J.E. Fischer, K.I. Winey, Electrical percolation behavior in silver nanowire-polystyrene composites: simulation and experiment, Adv. Funct. Mater. 20 (16) (2010) 2709–2716, https://doi.org/10.1002/adfm.201000451.
[41] N. Hu, Y. Karube, C. Yan, Z. Masuda, H. Fukunaga, Tunneling effect in a polymer/carbon nanotube nanocomposite strain sensor, Acta Mater. 56 (13) (2008) 2929–2936, https://doi.org/10.1016/j.actamat.2008.02.030.
[42] D. Eberly, Robust computation of distance between line segments [Online; accessed January 2019], https://www.geometrictools.com/Documentation/DistanceLine3Line3.pdf.
[43] T. Schilling, M.A. Miller, P. van der Schoot, Percolation in suspensions of hard nanoparticles: from spheres to needles, Europhys. Lett. 111 (5) (2015) 56004, https://doi.org/10.1209/0295-5075/111/56004.
[44] X. Zeng, X. Xu, P.M. Shenai, E. Kovalev, C. Baudot, N. Mathews, Y. Zhao, Characteristics of the electrical percolation in carbon nanotubes/polymer nanocomposites, J. Phys. Chem. C 115 (44) (2011) 21685–21690, https://doi.org/10.1021/jp207388n.
[45] L.-P. Simoneau, J. Villeneuve, C.M. Aguirre, R. Martel, P. Desjardins, A. Rochefort, Influence of statistical distributions on the electrical properties of disordered and aligned carbon nanotube networks, J. Appl. Phys. 114 (11) (2013) 114312, https://doi.org/10.1063/1.4821885.
[46] L. Schneider, C. Martin, Y. Bultel, D. Bouvard, E. Siebert, Discrete modelling of the electrochemical performance of SOFC electrodes, Electrochim. Acta 52 (1) (2006) 314–324, https://doi.org/10.1016/j.electacta.2006.05.018.
[47] A. Abbaspour, J.-L. Luo, K. Nandakumar, Three-dimensional random resistor-network model for solid oxide fuel cell composite electrodes, Electrochim. Acta 55 (12) (2010) 3944–3950, https://doi.org/10.1016/j.electacta.2010.02.049.
[48] K. Rhazaoui, Q. Cai, C.S. Adjiman, N.P. Brandon, Towards the 3D modeling of the effective conductivity of solid oxide fuel cell electrodes: I. Model development, Chem. Eng. Sci. 99 (2013) 161–170, https://doi.org/10.1016/j.ces.2013.05.030.
[49] K. Rhazaoui, Q. Cai, C.S. Adjiman, N.P. Brandon, Towards the 3D modeling of the effective conductivity of solid oxide fuel cell electrodes—II. computational parameters, Chem. Eng. Sci. 116 (2014) 781–792, https://doi.org/10.1016/j.ces.2014.05.045.
[50] K. Rhazaoui, Q. Cai, M. Kishimoto, F. Tariq, M.R. Somalu, C.S. Adjiman, N.P. Brandon, Towards the 3D modelling of the effective conductivity of solid oxide fuel cell electrodes — validation against experimental measurements and prediction of electrochemical performance, Electrochim. Acta 168 (2015) 139–147, https://doi.org/10.1016/j.electacta.2015.04.005.
[51] N. Nitta, F. Wu, J.T. Lee, G. Yushin, Li-ion battery materials: present and future, Mater. Today 18 (5) (2015) 252–264, https://doi.org/10.1016/j.mattod.2014.10.040.
[52] K.K. Showa Denko, Vapor grown carbon fiber [Online; accessed January 2019], http://www.sdk.co.jp/english/products/126/132/2094.html.
[53] A. Salvadori, E. Bosco, D. Grazioli, A computational homogenization approach for Li-ion battery cells: Part 1 – formulation, J. Mech. Phys. Solids 65 (2014) 114–137, https://doi.org/10.1016/j.jmps.2013.08.010.
[54] M. Dixit, H. Meyer, T. Schilling, Connectivity percolation in suspensions of attractive square-well spherocylinders, Phys. Rev. E 93 (2016), 012116, https://doi.org/10.1103/PhysRevE.93.012116.
[55] O. Toprakci, L. Ji, Z. Lin, H.A. Toprakci, X. Zhang, Fabrication and electrochemical characteristics of electrospun $LiFePO_4$/carbon composite fibers for lithium-ion batteries, J. Power Sources 196 (18) (2011) 7692–7699, https://doi.org/10.1016/j.jpowsour.2011.04.031.
[56] B. Wu, Y. Ren, N. Li, $LiFePO_4$ cathode material, in: S. Soylu (Ed.), Electric Vehicles: the Benefits and Barriers, IntechOpen, 2011, pp. 199–216, https://doi.org/10.5772/18995. Ch. 11.
[57] D. Grazioli, O. Verners, V. Zadin, D. Brandell, A. Simone, Electrochemical-mechanical modeling of solid polymer electrolytes: impact of mechanical stresses on Li-ion battery performance, Electrochim. Acta 296 (2018) 1122–1141, https://doi.org/10.1016/j.electacta.2018.07.234.
[58] European Commission, Become competitive in the global battery sector to drive e-mobility and stationary storage forward [Online; accessed January 2019], https://setis.ec.europa.eu/system/files/integrated_set-plan/action7_declaration_of_intent_0.pdf.
[59] I. Balberg, N. Binenbaum, N. Wagner, Percolation thresholds in the three-dimensional sticks system, Phys. Rev. Lett. 52 (1984) 1465–1468, https://doi.org/10.1103/PhysRevLett.52.1465.
[60] F. Du, J.E. Fischer, K.I. Winey, Effect of nanotube alignment on percolation conductivity in carbon nanotube/polymer composites, Phys. Rev. B 72 (2005) 121404, https://doi.org/10.1103/PhysRevB.72.121404.